

■ Hadean geodynamics inferred from time-varying $^{142}\text{Nd}/^{144}\text{Nd}$ in the early Earth rock record

N.S. Saji, K. Larsen, D. Wielandt, M. Schiller, M.M. Costa, M.J. Whitehouse,
M.T. Rosing, M. Bizzarro

■ Supplementary Information

The Supplementary Information includes:

- 1. Material and Methods
- 2. Supplementary Text
- Tables S-1 to S-5
- Figures S-1 to S-17
- Supplementary Information References

1. Material and Methods

1.1 Geological setting and sample description

The Isua supracrustal belt in SW Greenland is part of the Itsaq Gneiss Complex and represents one of the oldest and most well-preserved Archean terranes of the world. It is an ~35 km across, arcuate belt of meta-volcanic and meta-sedimentary rocks surrounded by abundant gneisses known regionally as Amitsoq gneisses. The detailed geology of the region is described elsewhere (Nutman and Friend, 2009). In short, the Isua supracrustal belt consists of amphibolite-facies mafic, ultramafic and felsic volcanic and sedimentary rocks. The minimum age of the supracrustal rocks is constrained by the tonalite sheets that are known to intrude the supracrustals based on cross-cutting field associations. Nutman and Friend (2009) recognise two terranes based on U-Pb ages; a northern terrain that formed at ~3.7 Ga and a southern terrain that formed at ~3.8 Ga, both sutured together by a dividing sedimentary unit that contains detrital zircons with ages up to ~3.9 Ga. Several low-strain areas in the belt preserve primary igneous characteristics such as pillow lava and sheeted dyke structures suggesting emplacement of these rocks in an intra-oceanic setting. The mafic rocks in the belt are recognised to be of two distinct geochemical affinities, that is, modern-day boninite-like metabasalts and metabasalts of island arc tholeiitic to picritic affinity. The Eoarchean (>3.6 Ga) mafic samples analysed in this study were collected largely from outcrops that preserve primary igneous features in the units with tholeiitic to picritic affinity on the western arm of the belt. The sample descriptions and GPS locations are given in Table S-1. The felsic rocks analysed include orthogneisses from the northern and southern Amitsoq gneiss terranes as well as tonalitic dykes that were found to directly intrude the metabasalts/amphibolites. The Ameralik dykes represent a mafic dyke swarm that intrude the Isua supracrustals in the Palaeoarchean at ~3.4 Ga (Rizo *et al.*, 2012). Our subset of Ameralik samples include both doleritic dykes from the southern terrain as well as noritic dykes from the northern terrain. The doleritic dykes were 1-20 cm wide and contained large (up to 5 cm) plagioclase phenocrysts in a fine to medium grained ground mass. The noritic dykes sampled, characterised by coarse-grained inner cores and fine-grained outer margins, were up to 100 m wide. The Ameralik dykes analysed were sampled from the same or nearby sample locations as in Rizo *et al.* (2012) in order to enable sample correspondence. The samples AM-1, AM-8, AM-9, AM-10,



AM-14 and AM-18 correspond to samples AM-006, 00-014, 00-015, AM-011, AM-012 and AM-004 of Rizo *et al.* respectively at the outcrop scale.

1.2 Analytical procedures

Approximately ~100 g rock chips from the bulk samples were hand-crushed and powdered using an agate ball mill. Care was taken to obtain fresh interior samples with minimal alteration effects. Major and trace element data was obtained on ~10 g homogenised powdered samples from Actlabs, Canada, by fusion ICP-MS (Table S2). Sample powders weighing 250-500 mg were dissolved in concentrated HF-HNO₃ mixture at 150 °C on a hotplate for two days. Repeated treatment with concentrated aqua regia and 6M HCl followed HF-HNO₃ digestion until a clear solution was obtained. In cases where residues were left after several steps involving aqua regia, the solution was centrifuged, and the supernatant carefully removed. The residue was pressure digested using HF-HNO₃ in Parr vessel bombs at 210 °C for two days following a ramp-up step at 150 °C for a day. The resulting solutions were dried down and treated with concentrated aqua regia and 6M HCl until complete dissolution was achieved. Subsequently, the dissolved residue was recombined with the supernatant. The Nd-purification scheme as well as MC-ICPMS analysis protocol is described in Saji *et al.* (2016). In short, Nd was purified from sample matrix in a three-step procedure. The REEs were first isolated as a group on a cation column. Ce was separated from Nd by oxidation using HBrO₃ and the other adjacent REEs were subsequently separated on an automated Ln-spec column by elution with 0.2M HCl. The Ce and Sm interference levels after purification chemistry were on average 15 and 10 ppm on ¹⁴²Nd and ¹⁴⁴Nd, respectively (Table S-3). Doping experiments demonstrate that the interference correction is robust within analytical reproducibility at this level of Ce and Sm (Saji *et al.*, 2016). Nd-isotope measurements were done on the Pandora Neptune Plus MC-ICPMS instrument at the Centre for Star and Planet Formation (University of Copenhagen) by sample-standard bracketing and isotope data is reported as parts per million deviations of the ¹⁴²Nd/¹⁴⁴Nd ratio from that of JNdi-1 standard, normalised to ¹⁴⁸Nd/¹⁴⁴Nd = 0.24157 and ¹⁴⁶Nd/¹⁴⁴Nd = 0.7219. We prefer the ¹⁴⁸Nd/¹⁴⁴Nd normalisation scheme as this provides better internal precision compared to ¹⁴⁶Nd/¹⁴⁴Nd conventionally used to report Nd-isotope data (Saji *et al.*, 2016). Samples were dissolved in 2 % HNO₃ and introduced into the plasma source *via* ESI Apex IR desolvating nebuliser at sample aspiration rates ranging from 0.05-0.08 mL/min. Samples were typically analysed at a ¹⁴²Nd intensity of 25 V or higher when possible. A single analysis consisted of 50-100 cycles with an integration interval of 8.34 s and each sample was analysed 10 times systematically. Total Nd procedural blanks were less than 100 pg which is negligible compared to the total amount of Nd processed for all samples. Approximately 1-2 % of the bulk sample digestions were separately spiked with ¹⁵⁰Nd-¹⁴⁹Sm mixed spike and ¹⁴⁷Sm/¹⁴⁴Nd ratios were measured by ID-MC-ICPMS. The REEs were separated on a miniature cation column and Sm and Nd fractions were obtained by elution with 0.25M HCl on a 10 × 0.4 cm Ln-spec column. The concentration of the mixed spike was determined by calibration against gravimetrically prepared normal Sm and Nd solutions whose concentrations were known to better than 0.1 %. The accuracy of the ¹⁴⁷Sm/¹⁴⁴Nd ratios is determined to be 1 % from the repeat analyses of BHVO-2 terrestrial standard. The Sm procedural blanks were better than 50 pg and negligible.

Two gneiss samples, GN-1 and GN-8, were selected for zircon U-Pb geochronology using the CAMECA IMS1280 SIMS instrument at the NordSIMS facility, Swedish Museum of Natural History (NRM), Stockholm. The samples were disaggregated with a jaw crusher and zircons were separated from the fraction inferior to 500 µm by standard mineral separation techniques, using a Frantz magnetic separator and heavy liquids. Zircon grains were further handpicked under a binocular microscope and about 80 to 100 euhedral, prismatic crystals of each sample were mounted in epoxy together with the 1065 Ma Geostandards 91500 zircon (Wiedenbeck *et al.*, 1995), polished and cathodoluminescence (CL) imaged prior to SIMS analysis using an ETP Semra CL detector mounted on a Philips XL30 SEM at NRM. Where distinctive in CL, cores were analysed, otherwise the central portion of apparently single phase grains were selected. Analytical procedures and instrument settings for the U-Pb SIMS analysis broadly follow those described by Whitehouse and Kamber (2005), with a 14 nA O₂ primary beam focused to extract secondary ion from a ~25 µm area, which were analysed at a mass resolution (M/ΔM) of 5400 and detected in a single ion counting electron multiplier. These analyses utilised a shortened procedure, measuring six cycles comprising the four stable Pb isotopes together with matrix species ⁹⁴Zr₂¹⁶O (used only for beam centering) and ²³⁸U¹⁶O₂. Pb isotope ratios were corrected for common Pb using the measured ²⁰⁴Pb signal and assuming the present-day model terrestrial Pb composition of Stacey and Kramers (1975). Pb/U ratios were calibrated relative to the standard using the relationship $^{206}\text{Pb}/^{238}\text{U} = k \cdot ^{206}\text{Pb}/^{238}\text{U}^{16}\text{O}_2$, where k is derived from the regularly interspersed standard analyses. Data are presented in Table S-4 and on inverse Concordia plots on Figure S-14.

2. Supplementary Text

2.1 Major and trace element systematics

We measured a total of 24 samples including Eoarchean amphibolites and Amitsoq orthogneisses as well as the Palaeoarchean



Ameralik dykes. The Eoarchean amphibolites analysed have tholeiitic basalt to basaltic andesite compositions with 52-64 wt. % SiO₂, 2.1-12.4 wt. % MgO, 6.9-15.7 wt. % Fe₂O₃ (total Fe), 1.7-6.0 wt. % Na₂O + K₂O, 4.2-10.6 wt. % CaO, 9.1-14.6 wt. % Al₂O₃, 0.5-1.5 wt. % TiO₂, 30-1230 ppm Cr and 20-380 ppm Ni. The CaO/Al₂O₃ ratios vary from 0.3 to 1.2 for the amphibolites whereas Al₂O₃/TiO₂ ratios range between 9.6 and 29.4. The amphibolites possess flat- to enriched-light REE (LREE) and middle REEs (MREE) chondrite-normalised patterns (La/Sm_n = 1.1-3.9 and Gd/Yb_n = 1.1-1.8) (Fig. S-1). Sample SD-2 with a highly enriched LREE pattern and 64 % SiO₂ represents an evolved magma of andesitic composition or, alternatively, indicates post-magmatic alteration by fluids derived from host gneisses. Most samples, except SD-2, show a significant correlation on diagrams of Zr *vs.* Al₂O₃, TiO₂, Nb and REE suggesting that the elemental abundances of SD-2 are affected by secondary processes (Fig. S-2). Covariation diagrams of some major and trace elements (*i.e.* Al, Ca, Ti and Cr) with MgO suggest preservation of magmatic trends to a certain degree (Fig. S-3). Magma segregation depths can be constrained to 2-4 GPa (60-125 km) based on Al₂O₃ and CaO/Al₂O₃ distributions (Fig. S-4). On a Gd/Yb_n *vs.* Al₂O₃/TiO₂ diagram, all Eoarchean amphibolites except SD-2 fall on the field occupied by Al-depleted Barberton-type komatiites indicating melting in the garnet stability field (Fig. S-5). The Al₂O₃/TiO₂ ratios show little correlation with Zr (Fig. S-3) suggesting that mantle source characteristics control Al/Ti rather than degree of melting. On primitive mantle-normalised diagrams, all Isua amphibolites are characterised by distinct depletion in Nb and Ti relative to Th or adjacent REE suggesting derivation from a metasomatised mantle enriched in subduction fluid-mobile elements (Fig. S-6).

The Ameralik dykes analysed of doleritic texture have largely homogeneous basaltic compositions indistinguishable from Isua amphibolites with 48-49 wt. % SiO₂, 6.3-7.6 wt. % MgO, 11.9-15.3 wt. % Fe₂O₃ (total Fe), 2.0-3.1 wt. % Na₂O + K₂O, 9.9-11.5 wt. % CaO, 14.1- 5.5 wt. % Al₂O₃, 0.8-1.4 wt. % TiO₂, 110-310 ppm Cr and 70-160 ppm Ni. The chondrite-normalised LREE and MREE patterns are slightly depleted to nearly flat respectively (La/Sm_n = 0.8-1.0 and Gd/Yb_n = 1.1-1.2). Sample AM17, a noritic dyke from the Northern Amitsoq gneiss terrain, show an LREE-enriched pattern (La/Sm_n = 2.3), higher SiO₂ (54 %), Th (1.1 ppm) as well as overall low abundance of MREE, HREE and HFSE (High Field Strength Elements) compared to metadoleritic dykes suggesting post-emplacement alteration by fluids from the surrounding gneisses. Except AM17, all Ameralik dykes show a systematic correlation of Zr with TiO₂, Nb and REE suggesting robustness of trace element signatures. Fractional crystallisation trends for the dykes could not be ascertained as the variability in MgO wt. % is rather limited. The CaO/Al₂O₃ ratios are highly homogeneous (0.72-0.77) suggesting magma segregation depths (2-3 GPa) similar to that of Isua Eoarchean amphibolites. On Gd/Yb_n *versus* Al₂O₃/TiO₂ diagram, Ameralik dykes fall on the Al-depleted field as the amphibolites but with somewhat lower Gd/Yb_n ratios suggesting lesser effect for garnet in the melt residue. On primitive mantle-normalised diagrams, Ameralik dykes do not show the Nb and Ti depletions that characterise Isua amphibolites suggesting derivation from a non-metasomatised N-MORB-like depleted mantle.

The Amitsoq gneisses analysed here have tonalite-granodiorite compositions with 63-71 wt. % SiO₂, 0.6-2.6 wt. % MgO, 1.6-4.4 wt. % CaO, 15.5-19.1 wt. % Al₂O₃, 2.6-5.9 wt. % Fe₂O₃ (total Fe) and Na₂O/K₂O between 1.3 to 10.4. The orthogneisses on chondrite-normalised diagrams have characteristically enriched LREE and MREE patterns (La/Sm_n = 2.4-8.9 and Gd/Yb_n = 1.6-4.7). On primitive mantle-normalised diagrams, Amitsoq gneisses show strong Nb and Ti depletions that mimic the Isua amphibolites suggesting a genetic relationship between the two rock suites. On a Zr/Nb *vs.* Nb/Th diagram used for discriminating mantle sources, Isua amphibolites and Amitsoq gneisses plot on the field of arc affinity given their characteristically lower Nb/Th ratios similar to upper continental crust (Fig. S-7). Ameralik dykes, on the other hand, have Nb/Th ratios similar to primitive mantle. The largely similar MORB-like Zr/Nb ratios of the Ameralik dykes and the Isua amphibolites suggest derivation from a similarly depleted mantle as Zr/Nb is a proxy for source depletion or enrichment when degree of melting is similar (Condie, 2003). On Nb/Yb *vs.* Th/Yb diagram, Ameralik dykes plot close to the MORB-OIB array between primitive mantle and N-MORB whereas Isua amphibolites show an oblique trend towards higher Th/Yb ratios consistent with input from crust-derived fluids or melts (Fig. S-8). On TiO₂/Yb *vs.* Nb/Yb diagram, both Ameralik dykes and Isua amphibolites plot very close to N-MORB with identical TiO₂/Yb and Nb/Yb ratios suggesting a similar depth of melting as well as source and melting characteristics (Fig. S-9).

2.2 Sm-Nd systematics

The ¹⁴⁷Sm-¹⁴³Nd systematics of our samples are plotted in Figures S-10 to S-13. The ¹⁴⁷Sm-¹⁴³Nd data for all Isua Eoarchean amphibolites yield a scattered array (MSWD = 9.7) with a slope corresponding to an age of 3644 ± 330 Myr (2σ; n = 9) and an intercept of 0.50794 ± 0.00038 that translates to an initial ε¹⁴³Nd of +0.70 ± 7.48 (2σ). The slope of the regression is largely controlled by sample SD-2 that show evidence for post-magmatic alteration and has the lowest ¹⁴⁷Sm/¹⁴⁴Nd ratio of 0.111 amongst mafic samples. Excluding this sample yields an age of 3340 ± 800 Myr consistent with the previous regression but with larger errors due to the very small spread in ¹⁴⁷Sm/¹⁴⁴Nd ratios. The ¹⁴⁷Sm-¹⁴³Nd data for the Amitsoq gneisses and tonalites yield a similar highly scattered array (MSWD = 21) with a slope corresponding to an age of 3330 ± 660 Myr (2σ; n = 7). Excluding the samples that fall off the regression line define an age of 3517 ± 350 Myr that agrees with the zircon U-Pb emplacement ages and an intercept of 0.50796 ± 0.00023 that translates to an initial ε¹⁴³Nd of -2.19 ± 4.53 (2σ). A combined regression of both mafic and felsic Eoarchean samples



yield a scattered array (MSWD = 17) with a slope corresponding to an age of 3772 ± 130 Myr (2σ ; $n = 16$) and an intercept of 0.50778 ± 0.00013 that translates to an initial $\epsilon^{143}\text{Nd}$ of $+0.86 \pm 2.56$ (2σ). This initial $\epsilon^{143}\text{Nd}$ value of $+0.86 \pm 2.56$ obtained represents the best estimate of initial $\epsilon^{143}\text{Nd}$ for the Isua Eoarchean rocks suites from Sm-Nd systematics in our study. This value agrees well with the precise initial $\epsilon^{143}\text{Nd}$ of $+2.0 \pm 1.6$ estimated from a well correlated Sm-Nd regression for a suite of felsic metasediments and micaschists ($n = 58$) from Moorbath *et al.* (1997). The ^{147}Sm - ^{143}Nd data for the Ameralik dykes yield a highly scattered array (MSWD = 20) with a slope corresponding to an age of 3646 ± 490 Myr (2σ ; $n = 10$) and an intercept of 0.50801 ± 0.00064 that translates to an initial $\epsilon^{143}\text{Nd}$ of $+2.12 \pm 12.60$ (2σ). The slope of the regression is largely controlled by sample AM-17 that has the lowest $^{147}\text{Sm}/^{144}\text{Nd}$ ratio of 0.127 and show evidence for contamination from host gneisses during emplacement. Sample AM-12 falls significantly above the regression suggesting REE mobility. Excluding the two samples yields a well-correlated regression (MSWD = 1.9; $n = 8$) with a slope corresponding to an age of 3148 ± 420 Myr (2σ) and an intercept of 0.50866 ± 0.00058 that translates to an initial $\epsilon^{143}\text{Nd}$ of $+2.08 \pm 11.41$ (2σ). The best estimates of initial $\epsilon^{143}\text{Nd}$ for the Eoarchean and Palaeoarchean rock suites are indistinguishable from each other within uncertainty.

2.3 U-Pb systematics of zircons from gneiss sample GN-1 and GN-8

Thirty-five zircon grains were analysed from sample GN-1, two of which were discarded from further consideration due to very high common Pb, probably from cracks or inclusions. Most analyses are concordant or near-concordant at ~ 3.8 Ga, with a few grains showing ancient Pb-loss along concordia together with some recent Pb-loss evident in the sub-horizontal discordance trends in Figure S-16. Applying a $<5\%$ discordance filter to minimise ambiguity related to the Pb-loss pattern, and rejecting the oldest analysis as possible inheritance, 13 grains yield a statistically significant weighted average $^{207}\text{Pb}/^{206}\text{Pb}$ age of 3803 ± 3 Ma (MSWD = 1.5, $p = 0.11$), interpreted as the likely crystallisation age of the gneiss.

Sixty-eight grains were analysed from sample GN-8, one of which was discarded as it sampled an inclusion. Most of the data are concordant or near-concordant at *ca.* 3.7 Ga, with some recent Pb-loss (sub-horizontal trend) evident in the concordia diagram (Fig. S-14). A number of grains, all slightly discordant, are dispersed towards older $^{207}\text{Pb}/^{206}\text{Pb}$ ages, suggesting some inheritance (up to a minimum age of ~ 3740 Ma based on the oldest $^{207}\text{Pb}/^{206}\text{Pb}$ age), which complicates determining an accurate age for this sample. Applying the same $<5\%$ discordance filter as in sample GN-1 limits the spread in ages, and rejecting the youngest ages as likely ancient Pb-loss dispersion along concordia, a coherent group of 26 $^{207}\text{Pb}/^{206}\text{Pb}$ ages yields a weighted average of 3701 ± 2 Ma (MSWD = 1.4, $p = 0.09$); an alternative, slightly less inclusive group of 23 oldest analyses in the $<5\%$ discordance group yields a weighted average of 3703 ± 3 Ma (MSWD = 1.3, $p = 0.16$, 1 rej.). These two alternatives cannot be separated on the basis of data and imaging, but an age of 3702 Ma is considered as the likely crystallisation age of the gneiss.

2.4 The $\mu^{142}\text{Nd}$ compositions of coeval mantle and comparison to literature data

The Nd-isotope compositions of the Isua samples analysed in the study are given in Table S-3. The Nd mass-dependent isotope variation *per* atomic mass unit, expressed as $\epsilon^{145}\text{Nd}$, are shown in Figure S-15. The mean $\epsilon^{145}\text{Nd}$ value for all the samples analysed in the study is -0.15 ± 0.11 ($n = 24$, 2 SE), indistinguishable within uncertainty from the mean $\epsilon^{145}\text{Nd}$ composition for terrestrial rock standards in Saji *et al.* (2016) (-0.24 ± 0.19). Two of the amphibolites analysed in the study, namely samples PB-1 and GB-1, have marginally fractionated $\epsilon^{145}\text{Nd}$ compositions outside the terrestrial composition, but return $\mu^{142}\text{Nd}$ compositions equivalent to 9.9 ± 1.6 and 10.7 ± 1.2 respectively, indistinguishable from the weighted mean of the $\mu^{142}\text{Nd}$ values of the amphibolites which is 10.5 ± 0.7 (2σ ; MSWD = 0.38). Moreover, the mass-independent $\mu^{145}\text{Nd}$, $\mu^{146}\text{Nd}$ and $\mu^{150}\text{Nd}$ values for the two samples are indistinguishable from terrestrial composition defined by JNdi-1 standard suggesting that any effect of mass-dependent fractionation is well-accounted for by the exponential law and that the measured $\mu^{142}\text{Nd}$ anomalies are not affected by inadequate mass fractionation correction. The mean mass-independent $\mu^{145}\text{Nd}$, $\mu^{146}\text{Nd}$ and $\mu^{150}\text{Nd}$ for the samples are -0.3 ± 0.6 , -0.6 ± 0.4 and -0.5 ± 1.3 ppm (95 % conf. err.) respectively, indistinguishable from the terrestrial composition. The $\mu^{142}\text{Nd}$ values from internal normalisation to both $^{148}\text{Nd}/^{144}\text{Nd}$ and $^{146}\text{Nd}/^{144}\text{Nd}$ are indistinguishable from each other within uncertainty further suggesting the robustness of the measurements.

The six Eoarchean Isua amphibolites we analysed have $\mu^{142}\text{Nd}$ compositions ranging from 8.9 ± 3.1 to 11.1 ± 2.4 whereas the metatonalites and Amitsoq orthogneisses define a mean $\mu^{142}\text{Nd}$ composition of 11.1 ± 0.7 (2σ ; MSWD = 0.5). The mean $\mu^{142}\text{Nd}$ composition of both rock suites are indistinguishable from the former. The variability within the Eoarchean Isua rocks in this study is lower by a factor of 3-6 compared to the spread in $\mu^{142}\text{Nd}$ compositions from earlier studies (Fig. S-16). Most of the early studies (Caro *et al.*, 2006; Bennett *et al.*, 2007) reported Nd isotope compositions relative to Ames Nd isotope standard whereas recent studies including ours report data relative to JNdi-1 Nd isotope standard which is indistinguishable from most terrestrial rocks standards. The mean $\mu^{142}\text{Nd}$ composition from Bennett *et al.* (2007) is higher than that of Caro *et al.* (2006) and this study by close to



5 ppm for both Amitsoq gneisses and ISB amphibolites. We also find no resolvable distinction within analytical uncertainty between the $\mu^{142}\text{Nd}$ signature of 3.8 Ga southern terrain and 3.7 Ga northern terrain tonalites/orthogneisses unlike the study of Bennett *et al.* (2007). We have shown in Saji *et al.* (2016) that Ames Nd carries a 2 ppm deficit in $\mu^{142}\text{Nd}$ relative to JNdi-1 due to equilibrium mass fractionation. For Amitsoq gneisses, accounting for this effect leads to a better agreement with our data for Bennett *et al.* (2007) while Caro *et al.* (2006) is offset towards lower compositions than originally. For amphibolites, correcting for standard difference on average brings the Bennett *et al.* (2007) values closer to that from this study while Caro *et al.* values remain similar within error. It is possible that different batches of Ames Nd have variable compositions, but this cannot entirely explain the discrepancies on the order of 5 ppm, at least for Bennett *et al.* (2007). Data relative to JNdi-1 from Rizo *et al.* (2011) for amphibolites is similar to ours on average but the total variability in the compositions range +2 ppm to +16 ppm, which we do not see in our study. The mean $\mu^{142}\text{Nd}$ we measure for Isua amphibolites and orthogneisses is identical to the mean of $\mu^{142}\text{Nd}$ values compiled from literature in O'Neil *et al.* (2016) that show a Gaussian distribution indicating that the spread in the existing dataset is primarily analytical scatter.

It is the Palaeoarchean ~3.4 Ga Ameralik dykes that show the highest distinction in comparison to the previous study of Rizo *et al.* (2012). Our sample set for Ameralik dykes includes mostly similar sample localities as in Rizo *et al.* (2012) and all the samples analysed in this study carry a well-resolved mean $\mu^{142}\text{Nd}$ excess of 4.9 ± 0.5 (2σ ; MSWD = 0.89) in contrast to the wide variability seen in the earlier data set. Despite major element covariations and trace element patterns suggesting sample correspondence between the two studies (section 2.1), we could not reproduce any of their negative $\mu^{142}\text{Nd}$ compositions, pointing to possible analytical artifacts in the data of Rizo *et al.* (2012). It is not possible to ascertain if the artefacts result from mass fractionation effects as the precision on other Nd isotopes (^{148}Nd and ^{150}Nd) is not sufficiently precise to resolve non-exponential mass fractionation patterns as in this study. The $\mu^{142}\text{Nd}$ values for a single sample (sample 00-014) measured in multiple sessions in Rizo *et al.* (2012) vary from -10.4 ± 4.6 to 4.6 ± 5.8 . Such a large variability in replicates point to the fact that Rizo *et al.* data is likely compromised by analytical artefacts. The result for AM-17, a noritic dyke that shows evidence for post-emplacement contamination from host-gneisses and record a $\mu^{142}\text{Nd}$ composition of 12.2 ± 2.6 in this study, is similar to that of Rizo *et al.* (2012). This could indicate that while the TIMS analytical technique used by Rizo *et al.* (2012) reasonably resolves anomalies on the order of 10 ppm, it fails to resolve anomalies on the order of 5 ppm that we measure in Ameralik dykes as it is close to the limit of their analytical precision.

The lack of correlation of $\mu^{142}\text{Nd}$ anomalies in Isua mantle-derived rocks with $^{147}\text{Sm}/^{144}\text{Nd}$ is well-established (Bennett *et al.*, 2007). The near-constant $\mu^{142}\text{Nd}$ compositions measured in this study for Isua mafic rocks that carry widely varying present-day $\mu^{143}\text{Nd}$ compositions (-2998 ppm to 721 ppm) and $^{147}\text{Sm}/^{144}\text{Nd}$ ratios (0.154 to 0.196) confirm the same and suggests that the measured anomalies represent an inherited $\mu^{142}\text{Nd}$ signature from the ambient mantle. The homogeneous $\mu^{142}\text{Nd}$ in the modern terrestrial mantle compared to the $\mu^{142}\text{Nd}$ heterogeneities in Archean rocks reflect the fact that mantle heterogeneities are erased over time by mantle stirring. In this framework, the $\mu^{142}\text{Nd}$ anomalies of lesser magnitude measured in the Palaeoarchean Ameralik dykes compared to the Eoarchean rock suites can be interpreted as homogenisation of Isua Hadean mantle reservoir with time by progressive mantle stirring. An unrelated possibility is that the ^{142}Nd signature carried by Ameralik dykes represents contamination from host gneisses during emplacement or effects of later metamorphism as there exists evidence for significant rare-earth element mobility in the Isua rocks (Rosing, 1990). If correct, mass balance arguments require ~10% contamination from the host gneisses to raise the ^{142}Nd signature of the dykes to the observed levels and the Ameralik dykes we sampled, except AM-17, do not show any evidence for LREE-enrichment and instead preserve flat to depleted LREE-patterns consistent with derivation from the ambient depleted mantle without any crustal contamination. The Ameralik dykes, except AM-17, also do not show the characteristic Nb-depletions on PM-normalised trace element diagrams that would be present if contaminated by gneiss-derived fluids. Thus, the homogeneous $\mu^{142}\text{Nd}$ recorded by the Ameralik dykes is interpreted as reflecting the isotopic signature of the coeval depleted mantle at ~3.45 Ga.

The possibility that Ameralik dykes sample a reservoir unrelated to the Isua Hadean depleted mantle that gave rise to the positive anomaly in 3.8 Ga rocks is unlikely on two fronts. One, the geochemistry of Ameralik dykes is consistent with derivation from the convecting upper mantle and does not point to plume-like or lithospheric sources. The Eoarchean rocks were sourced from a metasomatised wedge-like upper mantle. Though Ameralik dykes lack this characteristic, it could be that metasomatism by crust-derived fluids is a local process at the scale of large mantle domains such as this Hadean domain. Therefore, the most natural explanation for the subdued $\mu^{142}\text{Nd}$ anomaly in Ameralik dykes relative to Eoarchean rocks would that their $\mu^{142}\text{Nd}$ signatures correspond to progressive convective homogenisation of a Hadean depleted mantle domain. Secondly, the fact that bulk of the $\mu^{142}\text{Nd}$ anomalies from North Atlantic Craton and adjacent Superior Province are indeed related to a single large-scale differentiation of Hadean mantle (Fig. 2) makes derivation of Ameralik dykes in the ISB from an unrelated Hadean mantle domain unlikely.



2.5 Estimation of mantle stirring time

The reduced $\mu^{142}\text{Nd}$ anomaly in Palaeoarchean Ameralik dykes compared to the Eoarchean amphibolites define a homogenisation timescale for the Isua Hadean depleted mantle reservoir of ~ 1.4 Gyr and allows quantitative estimation of the mantle stirring rate in the Hadean-Archean period. The logic behind the above conclusion is as follows. Coupled ^{142}Nd - ^{143}Nd systematics of Isua Eoarchean rocks, assuming a two-stage evolution, constrain the time of formation of the Isua Hadean depleted mantle reservoir to $4.28^{+0.07}_{-0.07}$ Ga using ^{146}Sm half-life of 103 Myr or $4.40^{+0.06}_{-0.03}$ Ga using ^{146}Sm half-life of 68 Myr (Fig. S-17). Accepting that the $\mu^{142}\text{Nd}$ anomaly in Palaeoarchean Ameralik dykes represents the progressive convective homogenisation of this Hadean depleted mantle reservoir, extrapolating the decrease in ^{142}Nd anomaly from 10.5 ± 0.7 ppm at ~ 3.8 Ga to 4.9 ± 0.5 ppm by ~ 3.4 Ga predicts the $\mu^{142}\text{Nd}$ anomaly to be completely homogenised to modern accessible mantle composition by ~ 3.0 Ga. This defines an apparent homogenisation timescale of ~ 1.4 Gyr for the Hadean-Archean mantle, considering that the time of differentiation cannot be earlier than ~ 4.45 Ga or later than 4.39 Ga (Fig. 2 and Table S-5). The mantle stirring time (T_{stir}), defined as the time during which the variance in mantle compositional heterogeneity is reduced by a factor of e , is generally inferred from the dispersion in isotopic composition of mantle-derived samples. We have not attempted derivation of stirring time from the dispersion in Archean ^{142}Nd data as in Caro *et al.* (2006) as there are complications related to analytical artefacts in the literature data as outlined earlier. One way to work around this is by looking at how stirring times can be quantitatively related to homogenisation timescales so that the stirring rate corresponding to the homogenisation timescale we observe can be derived to compare with modern mantle stirring rate.

Kellogg *et al.* (2002) determine a stirring timescale of 250 – 750 Myr for modern convecting mantle from the isotopic dispersion seen in MORB. Following Kellogg *et al.* (2002), Jacobsen and Yu (2015) model the time evolution of distribution of ^{182}W isotope compositions for a given stirring rate and sampling length scale and this allows us to infer the relation between stirring timescales and homogenisation timescales albeit very crudely (Figs. 4-6). One can see from their time evolution plots that the bimodal distribution is homogenised after a timespan corresponding to 6 times the stirring time. This could be a conservative estimate as complete homogenisation into a single 0.1-epsilon bin is achieved only over 4.5 Gyr timespan for a stirring time of 0.5 Gyr, a factor of 9 as opposed to 6. The model of Jacobsen and Yu (2015) ignore the effects of radiogenic ingrowth which may not be applicable in the case of ^{142}Nd which has a longer half-life in comparison. Radiogenic ingrowth would result in heterogeneities being mixed away less rapidly. On the other hand, W -isotope heterogeneities at 2-epsilon levels would require much longer to be homogenised than Nd -isotope heterogeneities where the variance is on the order of 0.2-epsilon. Because these effects are counter balancing in nature, we consider the approximation that homogenisation timescales are longer than the stirring timescales by a factor of at least 6 or at most 9 to be fairly valid for ^{142}Nd variations. Thus, we infer that mantle stirring time (T_{stir}) can be related to the mantle homogenisation timescale T_{mix} via an empirical relation $T_{\text{stir}} \leq T_{\text{mix}}/x$ where $x = 6-9$ for basalt sampling scales of 30-100 km as shown in the mantle heterogeneity evolution plots of Jacobsen and Yu (2015). We arrive at a stirring timescale of $\sim 155 - 233$ Myr if we use the liberal and conservative estimates respectively. The ≤ 0.25 Gyr mantle stirring rate we infer for the Hadean-Archean mantle compared to mantle stirring timescale of $\sim 0.25-0.75$ Gyr estimated for the modern upper mantle (Kellogg *et al.*, 2002) in agreement with the theoretical predictions that Archean mantle convection must have been more rapid than today. Note that our interpretation of episodic stagnant lid tectonics in the early Earth (see section 2.5) derives from the crustal recycling rates we infer from the crust-mantle box model and is independent of the mantle stirring timescales presented above as tectonics of the planet is independent of mantle convection/dynamics.

2.6 Crust-mantle box model

The crust-mantle box model used to study the evolution of the mantle $\mu^{142}\text{Nd}$ evolution with time is based on Caro *et al.* (2006). Instead of the SCHEM model used in their study, however, we use a BSE model (present-day $\mu^{142}\text{Nd} = 0$ and $^{147}\text{Sm}/^{144}\text{Nd} = 0.196$) that is in agreement with the nucleosynthetic $\mu^{142}\text{Nd}$ excess on the modern terrestrial mantle relative to ordinary and carbonaceous chondrites (Burkhardt *et al.*, 2016). The box model takes into account the effect the crustal recycling in the evolution of the mantle $\mu^{142}\text{Nd}$ anomaly, which is ignored in the coupled ^{142}Nd - ^{143}Nd systematics. The three variables that control the magnitude of $\mu^{142}\text{Nd}$ anomaly in a mantle reservoir are time of differentiation, extent of Sm/Nd fractionation and rate of crustal recycling parameterised as crustal residence time. The temporal evolution of the mantle Nd -isotope anomaly as recorded in the Isua rocks allows us to constrain the three variables independent of each other using the crust-mantle box model. We consider Hadean differentiation times from 4.5 to 4.3 Ga as this covers the range of model ages within uncertainty estimated from coupled ^{142}Nd - ^{143}Nd systematics for Isua amphibolites. Batch melting with 5 and 20 % melt is considered to reflect high to low degrees of Sm/Nd fractionations, respectively. Hadean differentiation at 4.5 Ga results in inconsistency between crustal residence times inferred from ^{142}Nd and ^{143}Nd temporal evolution for both 5 and 20 % partial melting, defining an upper limit of ~ 4.45 Ga for the age of mantle differentiation (Table S-5). This is because the larger radiogenic ingrowth on ^{142}Nd when differentiation takes place early warrants



higher crustal recycling (*i.e.* short crustal residence times) to explain the relatively low measured $\mu^{142}\text{Nd}$ anomalies observed compared to the maximum ingrowth possible (~50 ppm) whereas such faster crustal recycling doesn't allow the initial $\varepsilon^{143}\text{Nd}$ values to grow to the observed radiogenic compositions unless crustal recycling rates are low. Hadean differentiation at ~4.4 Ga involving 20 % partial melting results in consistent crustal residence times (~2500 Myr) for both ^{142}Nd and ^{143}Nd evolution but the $\mu^{142}\text{Nd}$ anomalies predicted for the complementary crustal reservoir are lower than what is measured in the Nuvvuaqittuq and Ukaliq rocks. A differentiation event at ~4.4 Ga involving 5 % partial melting results in crustal residence times of ~1500 Myr generating $\mu^{142}\text{Nd}$ anomalies of up to -15 ppm, largely consistent with the Nuvvuaqittuq and Ukaliq data. Hadean differentiation at 4.3 Ga results in far lower radiogenic ingrowth (max. ingrowth of ~10 ppm) and fail to explain the observed $\mu^{142}\text{Nd}$ evolution.

Supplementary Tables

Table S-1 GPS locations for samples analysed in this study.

Sample ID	Type	GPS coordinates	
		Latitude	Longitude
PB-1	Pillow (meta)basalt	N 65°05'16.8"	W 50°10'29.0"
PB-2	Pillow (meta)basalt	N 65°05'20.1"	W 50°10'40.3"
PB-3	Pillow (meta)basalt	N 65°07'54.4"	W 50°09'48.5"
GB-1	Metagabbro	N 65°05'04.0"	W 50°09'54.9"
MG-1	Metagabbro	N 65°05'39.8"	W 50°11'00.1"
MG-2	Metagabbro	N 65°06'51.8"	W 50°09'45.7"
SD-2	Amphibolite	N 65°05'39.8"	W 50°11'00.1"
GN-1	Southern terrain gneiss	N 65°02'24.3"	W 50°14'18.3"
GN-3	Southern terrain gneiss	N 65°03'08.6"	W 50°13'44.3"
GN-4	Southern terrain gneiss	N 65°04'48.0"	W 50°10'37.1"
GN-7	Southern terrain gneiss	N 65°06'39.0"	W 50°07'57.9"
GN-8	Northern terrain gneiss	N 65°09'55.0"	W 49°58'05.0"
TN-1	Tonalilitic dyke	N 65°05'39.8"	W 50°11'00.1"
AM-1	Ameralik Dyke (Doleritic)	N 65°05'07.1"	W 50°09'34.5"
AM-2	Ameralik Dyke (Doleritic)	N 65°05'49.6"	W 50°09'36.2"
AM-8	Ameralik Dyke (Doleritic)	N 65°08'52.4"	W 50°10'05.5"
AM-9	Ameralik Dyke (Doleritic)	N 65°08'49.8"	W 50°10'13.3"
AM-10	Ameralik Dyke (Doleritic)	N 65°04'57.4"	W 50°10'32.3"
AM-12	Ameralik Dyke (Doleritic)	N 65°04'51.4"	W 50°10'25.4"
AM-14	Ameralik Dyke (Doleritic)	N 65°04'57.8"	W 50°09'58.7"
AM-16	Ameralik Dyke (Doleritic)	N 65°09'52.5"	W 49°57'55.9"
AM-17	Ameralik Dyke (Noritic)	N 65°09'53.9"	W 49°57'40.8"
AM-18	Ameralik Dyke (Doleritic)	N 65°06'33.3"	W 50°09'57.1"
PB-1	Pillow (meta)basalt	N 65°05'16.8"	W 50°10'29.0"
PB-2	Pillow (meta)basalt	N 65°05'20.1"	W 50°10'40.3"

Table S-2 Major and trace elements for samples analysed in this study.

Table S-2 is available for download as an Excel file at <http://www.geochemicalperspectivesletters.org/article1818>.

Table S-3 Nd isotope compositions and $^{147}\text{Sm}/^{144}\text{Nd}$ ratios measured for the SouthWest Greenland samples and terrestrial rock standards in this study.

Table S-3 is available for download as an Excel file at <http://www.geochemicalperspectivesletters.org/article1818>.



Table S-4 SIMS U-Th-Pb data from analysed zircon grains.

Sample ID	Comment	U ppm	Th/U _{calc} ¹	²⁰⁶ Pb/ ²⁰⁴ Pb	f ₂₀₆ (%) ²	Radiogenic (corrected) ratio ³				Calculated age ± σ (Ma)		Conc. (%)
						²⁰⁶ Pb/ ²³⁸ U ± σ (%)	²⁰⁷ Pb/ ²⁰⁶ Pb ± σ (%)	²⁰⁷ Pb/ ²⁰⁶ Pb	²⁰⁶ Pb/ ²³⁸ U	²⁰⁷ Pb/ ²⁰⁶ Pb	²⁰⁶ Pb/ ²³⁸ U	
GN-1, Southern terrain gneiss												
n5721_(GN-1)_@01		190	0.43	1970	0.95	0.7859	0.89	0.3591	0.22	3746 ± 3	3739 ± 25	99.7
n5721_(GN-1)_@02	incl. in wtd av.	210	0.58	140000	0.01	0.8424	0.98	0.3716	0.56	3798 ± 8	3939 ± 29	105
n5721_(GN-1)_@03		110	0.34	75000	0.02	0.7950	1.2	0.3699	0.45	3791 ± 7	3771 ± 36	99.3
n5721_(GN-1)_@04	incl. in wtd av.	120	0.37	106000	0.02	0.7848	1.2	0.3746	0.55	3810 ± 8	3734 ± 33	97.4
n5721_(GN-1)_@05		120	0.39	24100	0.08	0.7185	1.0	0.3726	0.30	3802 ± 5	3491 ± 27	89.4
n5721_(GN-1)_@06		3300	0.04	27700	0.07	0.7094	0.76	0.3317	0.24	3625 ± 4	3456 ± 20	94
n5721_(GN-1)_@07		190	0.58	11200	0.17	0.7708	1.4	0.3686	0.43	3786 ± 6	3684 ± 38	96.5
n5721_(GN-1)_@08		160	0.99	3380	0.55	0.7593	1.0	0.3721	0.28	3800 ± 4	3642 ± 29	94.5
n5721_(GN-1)_@09		400	0.34	13000	0.14	0.7936	0.93	0.3714	0.16	3797 ± 2	3766 ± 27	98.9
n5721_(GN-1)_@10	high PbC	140	1.10	211	8.87	0.7071	2.6	0.3636	5.4	3765 ± 82	3447 ± 71	89.1
n5721_(GN-1)_@11	incl. in wtd av.	120	0.65	23800	0.08	0.8000	0.85	0.3719	0.23	3799 ± 3	3789 ± 24	99.6
n5721_(GN-1)_@12	incl. in wtd av.	180	0.38	46600	0.04	0.7936	2.6	0.3795	1.2	3830 ± 19	3766 ± 75	97.8
n5721_(GN-1)_@13		3700	0.10	30100	0.06	0.6316	3.0	0.3120	3.7	3531 ± 57	3156 ± 75	86.6
n5721_(GN-1)_@14		110	1.10	72600	0.03	0.7786	0.87	0.3625	0.37	3760 ± 6	3712 ± 25	98.3
n5721_(GN-1)_@15		77	0.64	11100	0.17	0.7607	0.86	0.3710	0.94	3796 ± 14	3647 ± 24	94.9
n5721_(GN-1)_@16	incl. in wtd av.	220	0.50	22600	0.08	0.7815	1.3	0.3759	0.55	3815 ± 8	3723 ± 36	96.8
n5721_(GN-1)_@17		560	0.05	172000	0.01	0.7804	0.78	0.3571	0.38	3737 ± 6	3718 ± 22	99.3
n5721_(GN-1)_@18		120	0.41	10900	0.17	0.7335	1.7	0.3746	0.57	3810 ± 9	3546 ± 47	91
n5721_(GN-1)_@19		130	0.17	42000	0.04	0.7964	0.78	0.3681	0.21	3783 ± 3	3776 ± 22	99.8
n5721_(GN-1)_@20	incl. in wtd av.	330	0.58	144000	0.01	0.7880	2.7	0.3739	1.1	3807 ± 16	3746 ± 76	97.9
n5721_(GN-1)_@21	incl. in wtd av.	72	0.85	6860	0.27	0.7699	0.85	0.3731	0.31	3804 ± 5	3681 ± 24	95.7
n5721_(GN-1)_@22	incl. in wtd av.	59	0.56	>1e6	0	0.8024	0.80	0.3717	0.31	3798 ± 5	3798 ± 23	100
n5721_(GN-1)_@23		230	0.73	88900	0.02	0.7787	0.98	0.3802	0.67	3832 ± 10	3712 ± 28	95.9
n5721_(GN-1)_@24		51	0.67	62900	0.03	0.7979	0.90	0.3662	0.54	3776 ± 8	3781 ± 26	100.2
n5721_(GN-1)_@25	high PbC	560	0.06	215	8.68	0.4398	3.7	0.3510	0.34	3711 ± 5	2350 ± 74	56.5
n5721_(GN-1)_@26	incl. in wtd av.	100	1.00	97400	0.02	0.8059	0.78	0.3726	0.23	3802 ± 4	3810 ± 22	100.3
n5721_(GN-1)_@27		96	0.33	13200	0.14	0.8024	0.85	0.3676	0.61	3782 ± 9	3798 ± 24	100.6
n5721_(GN-1)_@28		340	0.36	2750	0.68	0.7488	0.85	0.3714	0.22	3797 ± 3	3603 ± 23	93.3
n5721_(GN-1)_@29		270	0.55	2410	0.78	0.7228	0.95	0.3668	0.18	3778 ± 3	3506 ± 26	90.7
n5721_(GN-1)_@30		360	0.98	984000	0	0.8446	0.80	0.3655	0.18	3773 ± 3	3947 ± 24	106.2
n5721_(GN-1)_@31	incl. in wtd av.	170	0.75	2290	0.82	0.7950	0.85	0.3720	0.22	3799 ± 3	3771 ± 24	99
n5721_(GN-1)_@32	incl. in wtd av.	84	0.59	29100	0.06	0.7847	0.89	0.3769	0.46	3819 ± 7	3734 ± 25	97.1
n5721_(GN-1)_@33	incl. in wtd av.	220	0.32	98000	0.02	0.8112	0.80	0.3732	0.16	3804 ± 2	3829 ± 23	100.9



Sample ID	Comment	U ppm	Th/U _{calc} ¹	²⁰⁶ Pb/ ²⁰⁴ Pb	f ₂₀₆ (%) ²	Radiogenic (corrected) ratio ³				Calculated age ± σ (Ma)		Conc. (%)
						²⁰⁶ Pb/ ²³⁸ U ± σ (%)	²⁰⁷ Pb/ ²⁰⁶ Pb ± σ (%)	²⁰⁶ Pb/ ²³⁸ U	²⁰⁷ Pb/ ²⁰⁶ Pb			
n5721_(GN-1)_@34		1200	0.48	2860	0.65	0.6810	1.9	0.3733	0.37	3805 ± 6	3348 ± 49	84.7
n5721_(GN-1)_@35	incl. in wtd av.	75	0.79	49600	0.04	0.8040	0.79	0.3748	0.27	3811 ± 4	3803 ± 23	99.7
GN-8, Northern terrain gneiss												
n5722_(GN-8)_@01		310	0.64	70400	0.03	0.7419	0.77	0.3463	0.14	3691 ± 2	3577 ± 21	96
n5722_(GN-8)_@02		230	0.54	140000	0.01	0.7645	0.87	0.3468	0.24	3693 ± 4	3661 ± 24	98.9
n5722_(GN-8)_@03	incl. in wtd av.1&2	240	0.73	11400	0.16	0.7480	0.91	0.3487	0.17	3701 ± 3	3600 ± 25	96.4
n5722_(GN-8)_@04	incl. in wtd av.1&2	79	0.54	2610	0.72	0.7596	0.85	0.3494	0.36	3705 ± 6	3643 ± 24	97.8
n5722_(GN-8)_@05		120	0.31	78300	0.02	0.7585	0.97	0.3450	0.23	3685 ± 4	3639 ± 27	98.3
n5722_(GN-8)_@06		220	0.81	2820	0.66	0.7162	1.1	0.3442	0.19	3681 ± 3	3482 ± 29	93
n5722_(GN-8)_@07	incl. in wtd av.1&2	130	0.49	26700	0.07	0.7397	0.89	0.3498	0.24	3706 ± 4	3569 ± 24	95.2
n5722_(GN-8)_@08	incl. in wtd av.1&2	150	0.31	35000	0.05	0.7602	0.81	0.3485	0.20	3701 ± 3	3645 ± 23	98
n5722_(GN-8)_@09		170	0.58	10600	0.18	0.6161	1.4	0.3462	0.22	3690 ± 3	3095 ± 35	79.7
n5722_(GN-8)_@10		230	1.60	332	5.64	0.5263	2.0	0.3543	0.36	3726 ± 5	2726 ± 46	67.3
n5722_(GN-8)_@11		250	0.28	112000	0.02	0.7524	0.77	0.3520	0.16	3715 ± 2	3616 ± 21	96.5
n5722_(GN-8)_@12		510	0.83	26200	0.07	0.7147	1.0	0.3561	0.21	3733 ± 3	3476 ± 27	91.1
n5722_(GN-8)_@13		200	0.58	10300	0.18	0.5194	2.7	0.3438	0.36	3680 ± 6	2697 ± 60	67.5
n5722_(GN-8)_@14	incl. in wtd av.1&2	160	0.49	23200	0.08	0.7459	0.77	0.3481	0.20	3699 ± 3	3592 ± 21	96.3
n5722_(GN-8)_@15		140	0.44	7410	0.25	0.6950	1.3	0.3548	0.47	3728 ± 7	3402 ± 35	88.8
n5722_(GN-8)_@16		170	0.53	35000	0.05	0.7635	0.85	0.3462	0.21	3690 ± 3	3657 ± 24	98.8
n5722_(GN-8)_@17	incl. in wtd av.1	210	0.70	7510	0.25	0.7377	1.1	0.3477	0.29	3697 ± 4	3562 ± 29	95.3
n5722_(GN-8)_@18		180	0.49	3240	0.58	0.6904	1.5	0.3473	0.37	3695 ± 6	3384 ± 39	89.2
n5722_(GN-8)_@19		210	0.47	4090	0.46	0.6858	0.78	0.3485	0.20	3700 ± 3	3367 ± 20	88.4
n5722_(GN-8)_@20	incl. in wtd av.1&2	410	0.57	4000	0.47	0.7409	0.83	0.3484	0.13	3700 ± 2	3574 ± 23	95.6
n5722_(GN-8)_@21		140	0.60	14600	0.13	0.7124	0.92	0.3528	0.34	3719 ± 5	3468 ± 25	91.3
n5722_(GN-8)_@22		1100	0.21	51000	0.04	0.7440	0.76	0.3368	0.14	3648 ± 2	3585 ± 21	97.8
n5722_(GN-8)_@23		150	0.61	3030	0.62	0.7322	0.91	0.3446	0.30	3683 ± 5	3542 ± 25	95
n5722_(GN-8)_@24	incl. in wtd av.1&2	130	0.77	79900	0.02	0.7700	0.90	0.3483	0.39	3700 ± 6	3681 ± 25	99.3
n5722_(GN-8)_@25		150	0.93	1950	0.96	0.6663	0.87	0.3413	0.23	3669 ± 3	3291 ± 22	86.9
n5722_(GN-8)_@26	incl. in wtd av.1&2	680	0.41	311000	0.01	0.7764	0.80	0.3478	0.10	3697 ± 2	3704 ± 23	100.2
n5722_(GN-8)_@27		270	1.30	2010	0.93	0.7544	1.3	0.3467	0.24	3693 ± 4	3624 ± 36	97.6
n5722_(GN-8)_@28		310	0.62	26400	0.07	0.6582	0.85	0.3557	0.15	3732 ± 2	3260 ± 22	83.9
n5722_(GN-8)_@29	incl. in wtd av.1&2	170	0.40	311000	0.01	0.7670	0.82	0.3488	0.19	3702 ± 3	3670 ± 23	98.9
n5722_(GN-8)_@30	incl. in wtd av.1&2	230	0.65	128000	0.01	0.7676	0.83	0.3485	0.23	3701 ± 4	3672 ± 23	99
n5722_(GN-8)_@31		83	0.18	11500	0.16	0.7610	0.83	0.3460	0.36	3690 ± 6	3648 ± 23	98.5
n5722_(GN-8)_@32	incl. in wtd av.1&2	210	0.40	119000	0.02	0.7941	0.94	0.3482	0.32	3699 ± 5	3768 ± 27	102.5
n5722_(GN-8)_@33	incl. in wtd av.1&2	360	0.87	3980	0.47	0.7474	0.82	0.3496	0.20	3705 ± 3	3598 ± 23	96.2
n5722_(GN-8)_@34		75	1.20	1120	1.66	0.7122	0.85	0.3459	0.34	3689 ± 5	3467 ± 23	92.2



Sample ID	Comment	U ppm	Th/U _{calc} ¹	²⁰⁶ Pb/ ²⁰⁴ Pb	f ₂₀₆ (%) ²	Radiogenic (corrected) ratio ³				Calculated age ± σ (Ma)		Conc. (%)
						²⁰⁶ Pb/ ²³⁸ U ± σ (%)	²⁰⁷ Pb/ ²⁰⁶ Pb ± σ (%)	²⁰⁷ Pb/ ²⁰⁶ Pb	²⁰⁶ Pb/ ²³⁸ U	²⁰⁷ Pb/ ²⁰⁶ Pb	²⁰⁶ Pb/ ²³⁸ U	
n5722_(GN-8)_@35	incl. in wtd av.1	320	0.72	1190	1.57	0.7488	0.88	0.3476	0.18	3697 ± 3	3603 ± 24	96.7
n5722_(GN-8)_@36	incl. in wtd av.1&2	230	0.89	5670	0.33	0.7617	0.86	0.3487	0.25	3701 ± 4	3650 ± 24	98.2
n5722_(GN-8)_@37		100	0.37	123000	0.02	0.7230	1.4	0.3553	0.45	3730 ± 7	3507 ± 39	92.3
n5722_(GN-8)_@38		150	0.41	19400	0.1	0.6074	0.84	0.3456	0.24	3688 ± 4	3059 ± 21	78.7
n5722_(GN-8)_@39		190	0.41	21400	0.09	0.7513	0.93	0.3465	0.18	3692 ± 3	3612 ± 26	97.2
n5722_(GN-8)_@40		390	0.51	7820	0.24	0.6580	0.76	0.3540	0.32	3724 ± 5	3259 ± 19	84.1
n5722_(GN-8)_@41	incl. in wtd av.1&2	110	0.59	51900	0.04	0.7635	0.78	0.3482	0.24	3699 ± 4	3657 ± 22	98.5
n5722_(GN-8)_@42	incl. in wtd av.2	320	0.37	112000	0.02	0.7652	0.77	0.3510	0.14	3712 ± 2	3663 ± 22	98.3
n5722_(GN-8)_@43		300	0.58	46300	0.04	0.7254	1.8	0.3544	0.64	3726 ± 10	3516 ± 49	92.7
n5722_(GN-8)_@44		450	0.67	1060	1.76	0.5217	2.4	0.3314	0.99	3624 ± 15	2707 ± 53	69.2
n5722_(GN-8)_@45		190	0.43	51500	0.04	0.7543	0.84	0.3448	0.18	3684 ± 3	3623 ± 23	97.8
n5722_(GN-8)_@46	incl. in wtd av.1&2	91	0.47	97200	0.02	0.7657	0.84	0.3479	0.26	3698 ± 4	3665 ± 23	98.8
n5722_(GN-8)_@47	incl. in wtd av.1&2	99	0.59	184000	0.01	0.7602	0.82	0.3485	0.24	3700 ± 4	3645 ± 23	98
n5722_(GN-8)_@48	incl. in wtd av.1	120	0.69	1850	1.01	0.7403	0.84	0.3476	0.33	3697 ± 5	3572 ± 23	95.6
n5722_(GN-8)_@49		170	0.64	35800	0.05	0.7742	2.5	0.3430	1.2	3676 ± 18	3696 ± 72	100.7
n5722_(GN-8)_@50		160	0.43	107000	0.02	0.7728	1.7	0.3463	0.48	3691 ± 7	3691 ± 47	100
n5722_(GN-8)_@51		140	0.42	260000	0.01	0.7710	0.82	0.3458	0.21	3689 ± 3	3684 ± 23	99.8
n5722_(GN-8)_@52	incl. in wtd av.1&2	87	0.26	44300	0.04	0.7825	0.78	0.3486	0.26	3701 ± 4	3726 ± 22	100.9
n5722_(GN-8)_@54	incl. in wtd av.1&2	340	0.60	9410	0.2	0.7584	0.81	0.3484	0.13	3700 ± 2	3638 ± 22	97.8
n5722_(GN-8)_@55	incl. in wtd av.1	630	0.99	28500	0.07	0.7799	0.98	0.3473	0.41	3695 ± 6	3717 ± 28	100.8
n5722_(GN-8)_@56	incl. in wtd av.1&2	380	0.39	44000	0.04	0.7502	0.78	0.3495	0.13	3705 ± 2	3608 ± 22	96.6
n5722_(GN-8)_@57	incl. in wtd av.1&2	220	0.43	45000	0.04	0.7458	0.78	0.3502	0.17	3708 ± 3	3592 ± 22	95.9
n5722_(GN-8)_@58	incl. in wtd av.2	190	0.44	75600	0.02	0.7433	0.83	0.3507	0.20	3710 ± 3	3583 ± 23	95.5
n5722_(GN-8)_@59		140	0.48	46800	0.04	0.7304	0.77	0.3467	0.22	3693 ± 3	3535 ± 21	94.5
n5722_(GN-8)_@61	incl. in wtd av.2	240	0.59	8610	0.22	0.7626	0.78	0.3514	0.49	3713 ± 7	3654 ± 22	97.9
n5722_(GN-8)_@62		140	0.67	6040	0.31	0.7119	0.81	0.3477	0.24	3697 ± 4	3466 ± 22	91.9
n5722_(GN-8)_@63	incl. in wtd av.1&2	230	0.47	4040	0.46	0.7410	0.87	0.3502	0.18	3708 ± 3	3574 ± 24	95.3
n5722_(GN-8)_@64		180	0.72	10900	0.17	0.7099	1.9	0.3437	0.42	3679 ± 6	3458 ± 52	92.2
n5722_(GN-8)_@65		230	0.49	87400	0.02	0.7813	1.1	0.3467	0.41	3692 ± 6	3722 ± 32	101
n5722_(GN-8)_@66		320	0.82	11000	0.17	0.6555	0.78	0.3472	0.16	3695 ± 2	3250 ± 20	84.7
n5722_(GN-8)_@67		390	0.37	2490	0.75	0.6718	2.0	0.3573	0.81	3738 ± 12	3313 ± 51	85.5
n5722_(GN-8)_@69		230	0.48	23100	0.08	0.7089	1.2	0.3483	0.59	3700 ± 9	3454 ± 32	91.5
n5722_(GN-8)_@70	incl. in wtd av.1&2	89	0.50	116000	0.02	0.7626	0.86	0.3491	0.32	3703 ± 5	3654 ± 24	98.3

(1) Calculated from ²⁰⁸Pb/²⁰⁶Pb ratio and age, assuming concordance

(2) f₂₀₆ is the percentage of common Pb estimated from ²⁰⁴Pb counts; in parentheses where these are insignificant

(3) Ratios after subtraction of common Pb



Table S-5 Crust residence times and $\mu^{142}\text{Nd}$, $\epsilon^{143}\text{Nd}$ values inferred for the crust using the crust-mantle box model for Archean rocks (excluding Theo's Flow) for different model input parameters - time of differentiation (T) and percentage of melting (F).

(Time (Ga), F (%))	Crustal residence time inferred from $\mu^{142}\text{Nd}$ evolution	Crustal residence time inferred from $\epsilon^{143}\text{Nd}$ evolution	$\mu^{142}\text{Nd}$ crust	$\epsilon^{143}\text{Nd}$ crust	Max $\mu^{142}\text{Nd}$ ingrowth
(4.5, 0.05)	750 - 1000	1000 - 4000	-30	-4	40
(4.5, 0.20)	1250 - 1750	2000 - 6000	-5	-1	40
(4.4, 0.05)	1000 - 1500	1000 - 4000	-15	-4	20
(4.4, 0.20)	2000 - 3000	2000 - 6000	-2	-1	20
(4.3, 0.05)	2000 - 5000	1000 - 4000	-8	-2	10
(4.3, 0.20)	4000 - 6000	2000 - 6000	-1	-0.5	10

Supplementary Figures

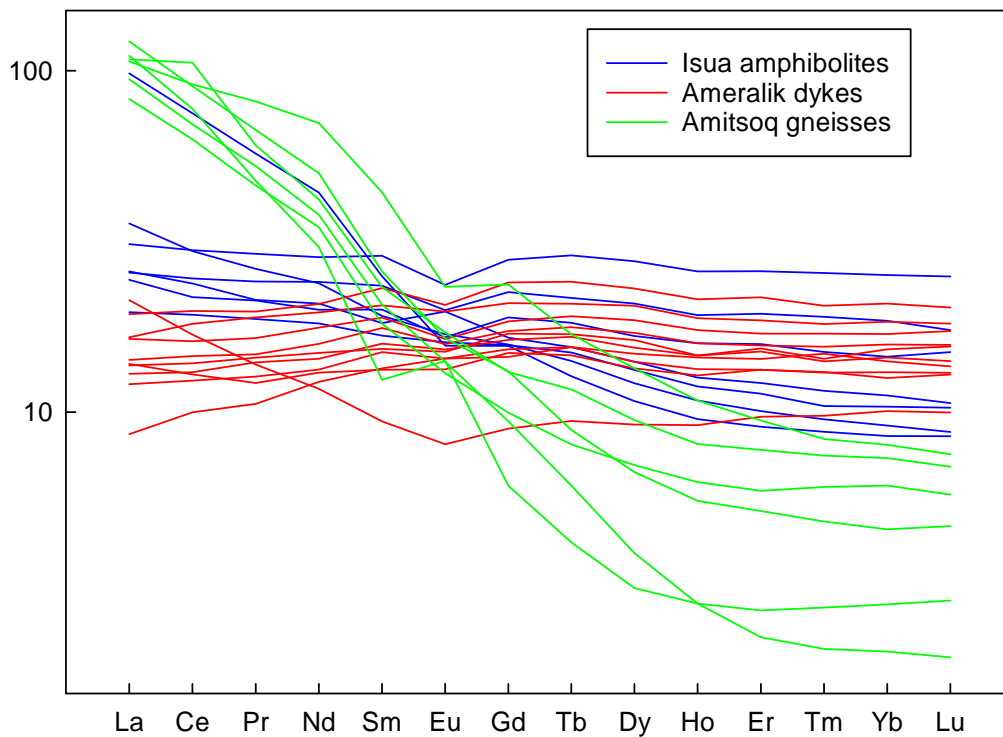


Figure S-1 Rare earth element patterns for rocks analysed in the study. Element concentrations are normalised to the CI chondrite composition (McDonough and Sun, 1995).



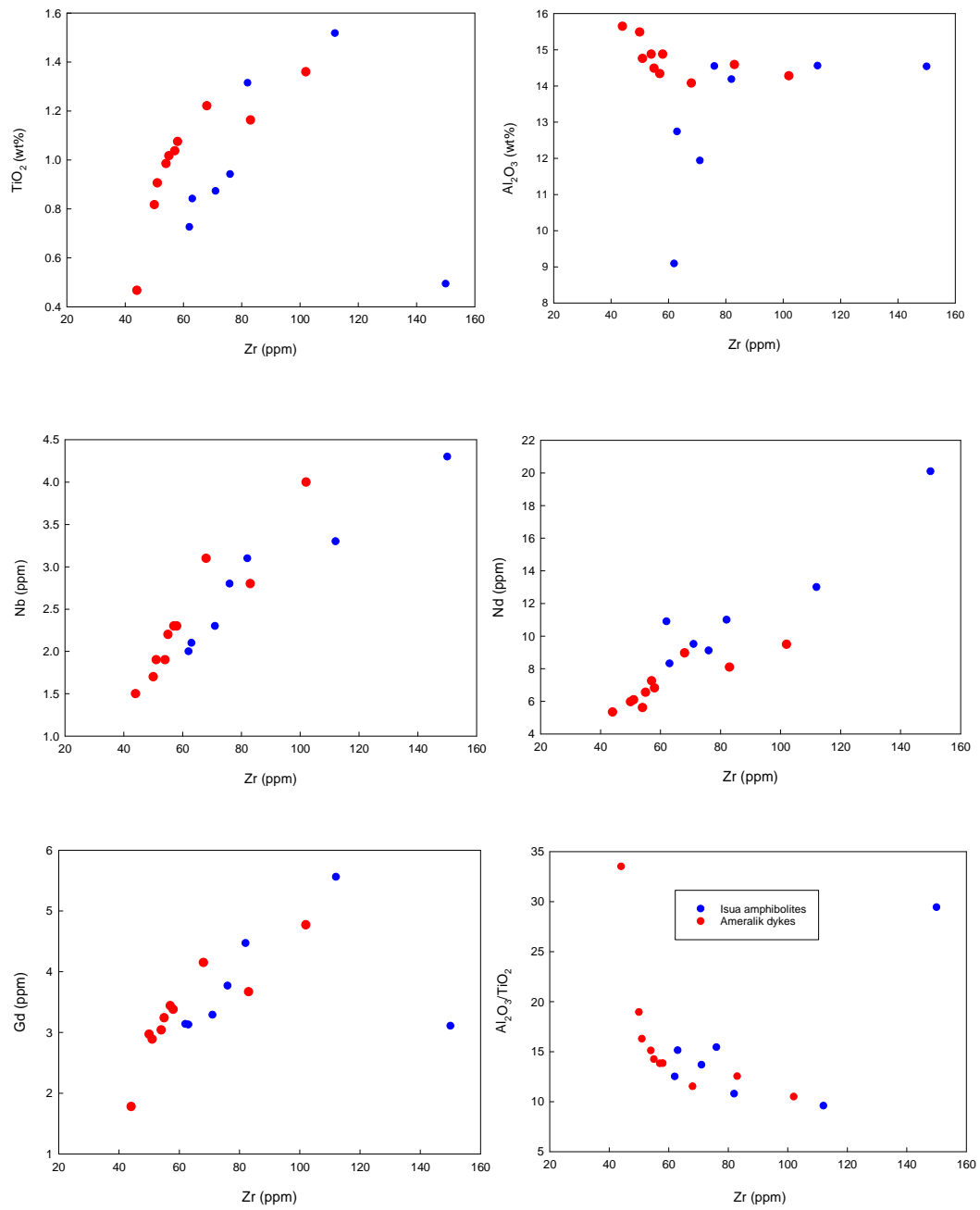


Figure S-2 Zr vs. selected element variations to illustrate the mobility of elements in Isua rocks analysed.



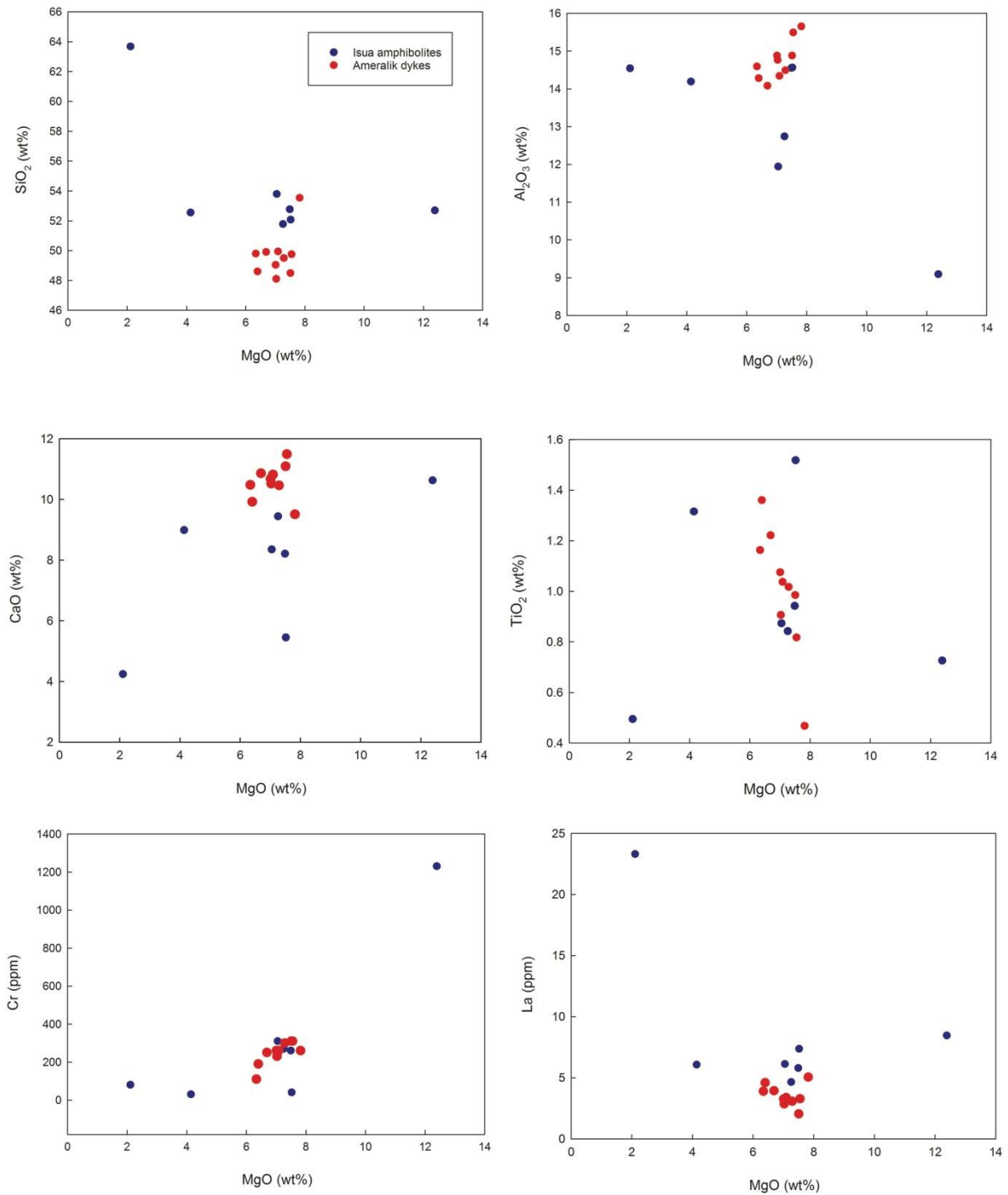


Figure S-3 MgO covariation diagrams for Isua amphibolites and Ameralik dykes analysed in the study.



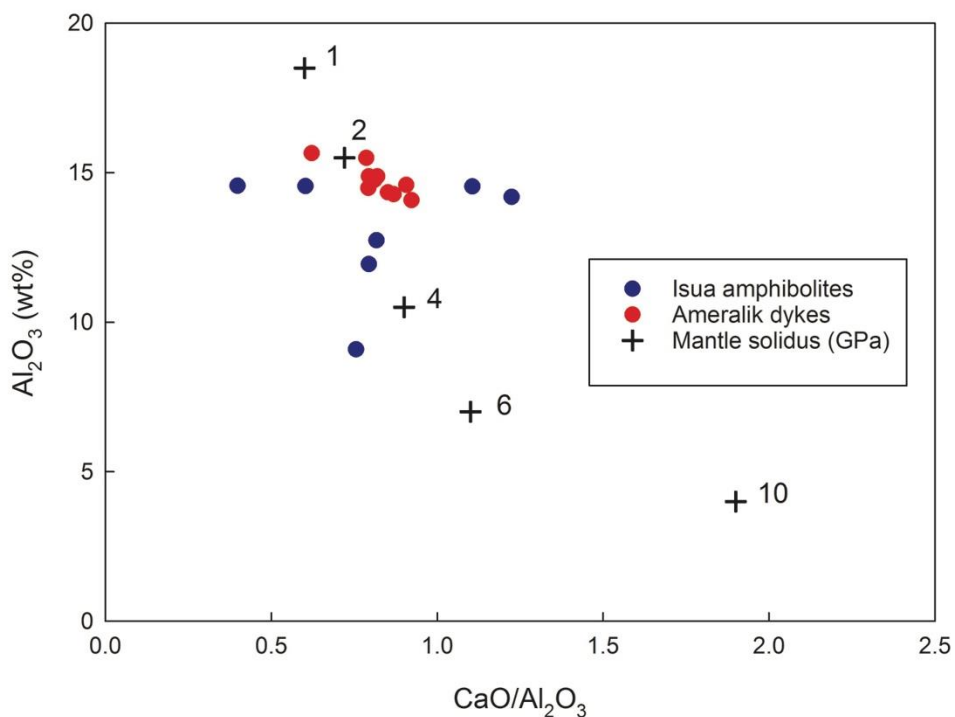


Figure S-4 Al_2O_3 vs. CaO/Al_2O_3 diagram for Isua amphibolites and Ameralik dykes. Melt segregation depths in GPa inferred from the mantle solidus is also shown (Condie, 2003).

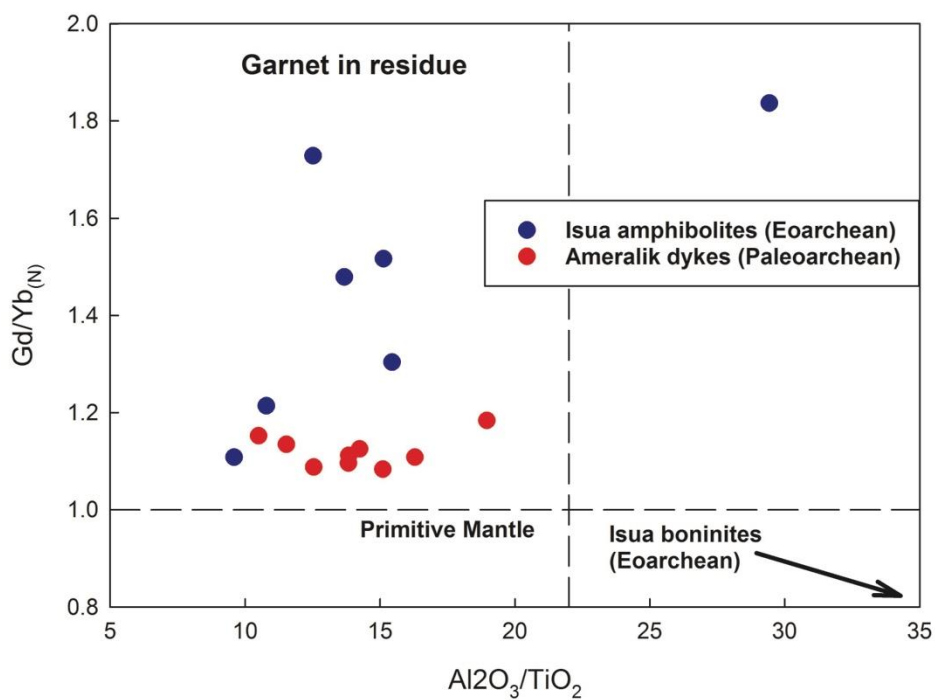


Figure S-5 $Gd/Yb_{(N)}$ vs. Al_2O_3/TiO_2 diagram for Isua amphibolites and Ameralik dykes indicating derivation of both by melting in the garnet stability field. Data for Isua boninites after Polat *et al.* (2002).



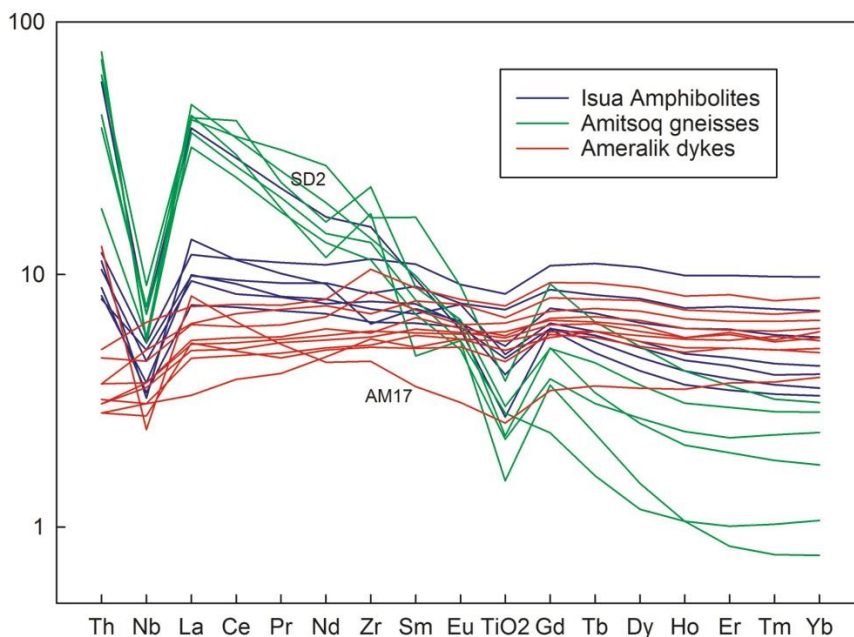


Figure S-6 Primitive-mantle normalised trace element patterns for rocks analysed in the study.

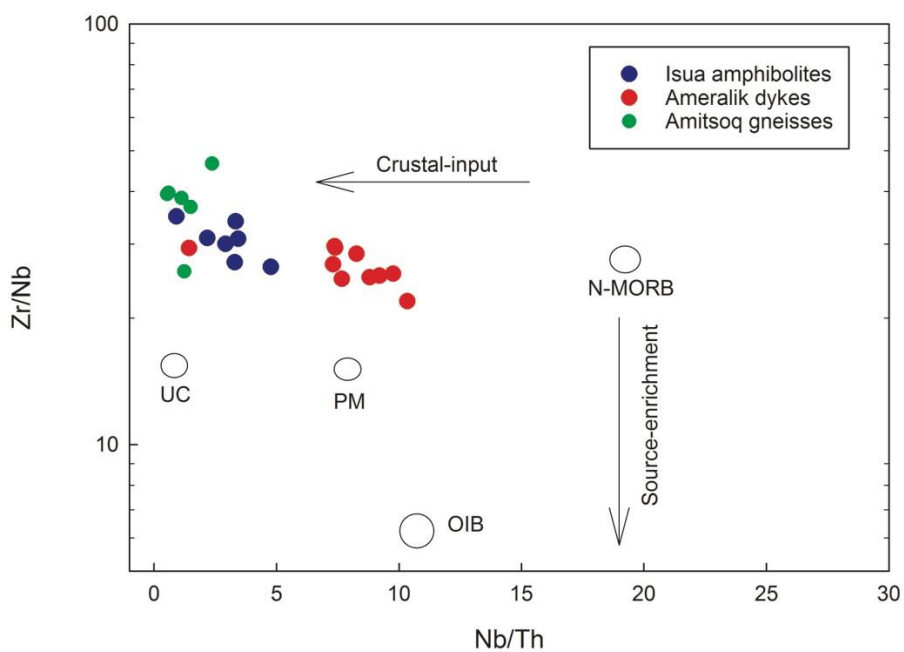


Figure S-7 Zr/Nb vs. Nb/Th diagram for Isua rocks indicating the depleted character of mantle sources of both Isua amphibolites and Ameralik dykes (similar Zr/Nb). Isua amphibolites (and Amitsoq gneisses) have lower Nb/Th ratios suggesting the presence of recycled crustal components in their source (Condie, 2003).



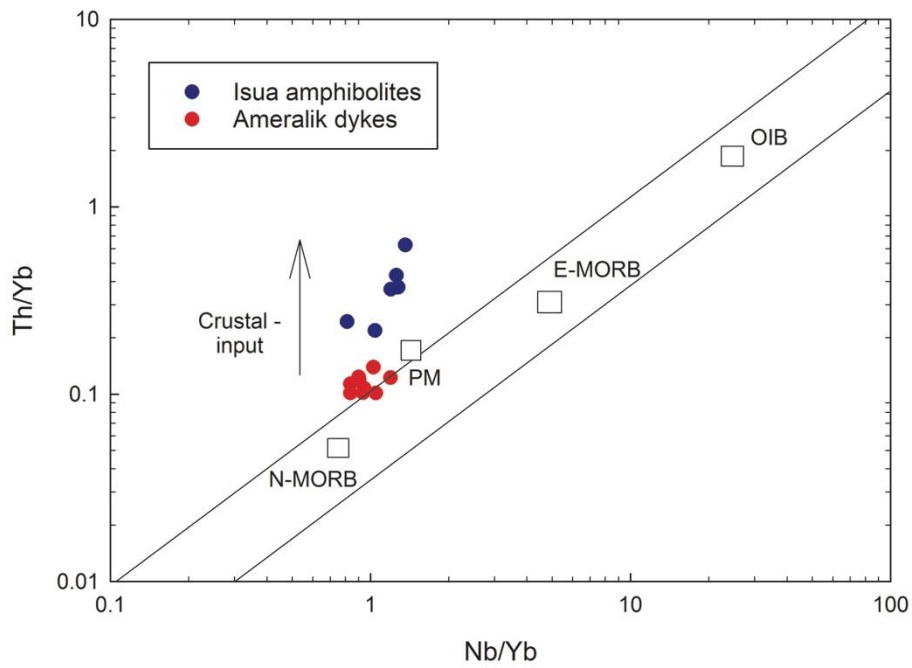


Figure S-8 Th/Yb vs Nb/Yb diagram for Isua rocks indicating the arc-like signature of Isua amphibolites while Ameralik dykes plot close to the MORB-OIB array (Pearce, 2008).

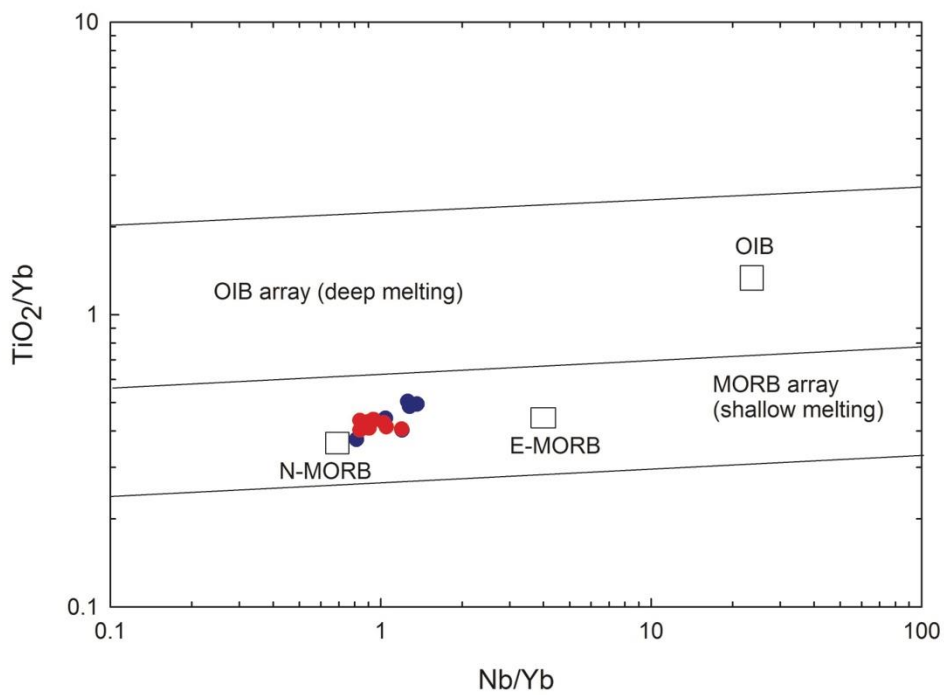


Figure S-9 Ti/Yb vs Nb/Yb diagram for Isua amphibolites and Ameralik dykes indicating derivation from melting of shallow MORB-like mantle (Pearce, 2008).



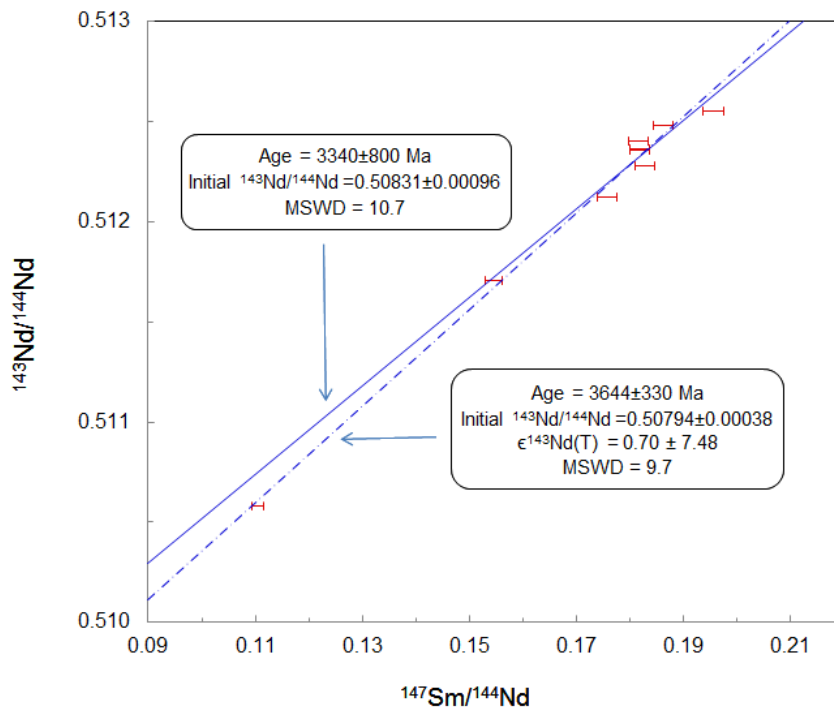


Figure S-10 $^{143}\text{Nd}/^{144}\text{Nd}$ vs. $^{147}\text{Sm}/^{144}\text{Nd}$ diagram for Isua amphibolites. Sample SD-2 with the lowest $^{147}\text{Sm}/^{144}\text{Nd}$ ratio of 0.12 is excluded in the regression given by solid line.

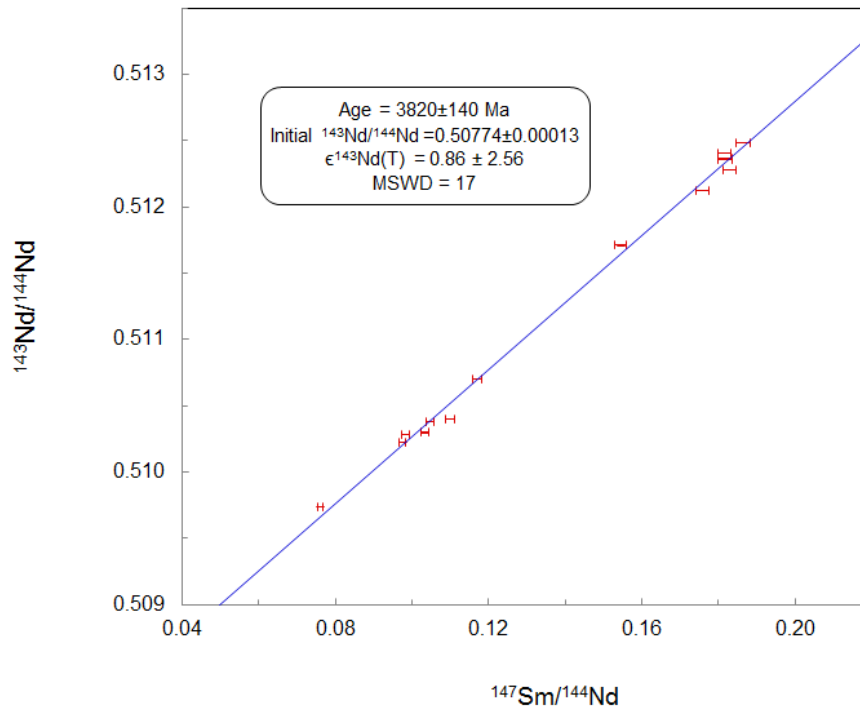


Figure S-11 $^{143}\text{Nd}/^{144}\text{Nd}$ vs. $^{147}\text{Sm}/^{144}\text{Nd}$ diagram for combined regression of both Isua amphibolites and Amitsoq gneisses that yield ages consistent with U-Pb emplacement ages of gneisses.



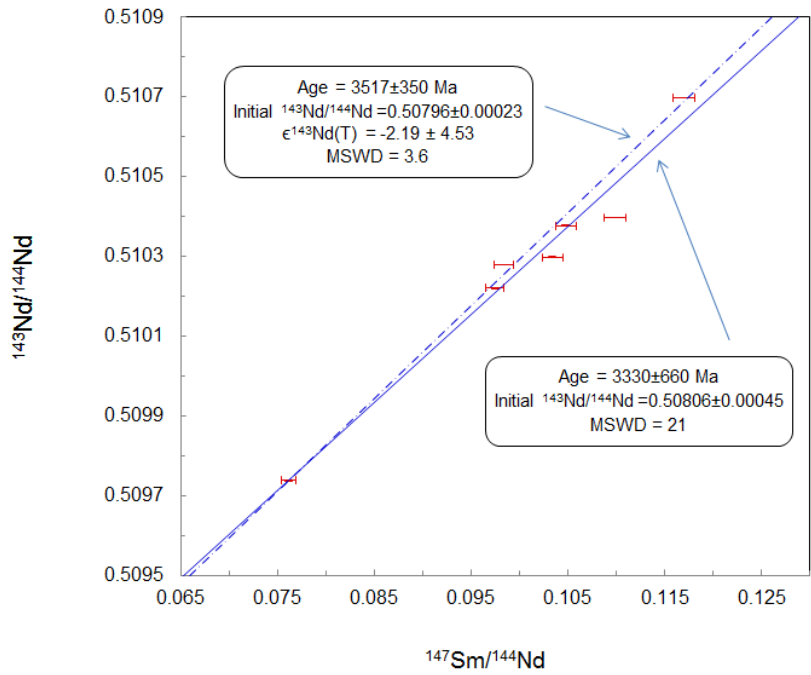


Figure S-12 $^{143}\text{Nd}/^{144}\text{Nd}$ vs. $^{147}\text{Sm}/^{144}\text{Nd}$ diagram for all Amitsoq gneisses (solid line) that show a high degree of scatter. Excluding the samples that fall off the regression line improves the MSWD but define ages younger than the U-Pb emplacement ages.

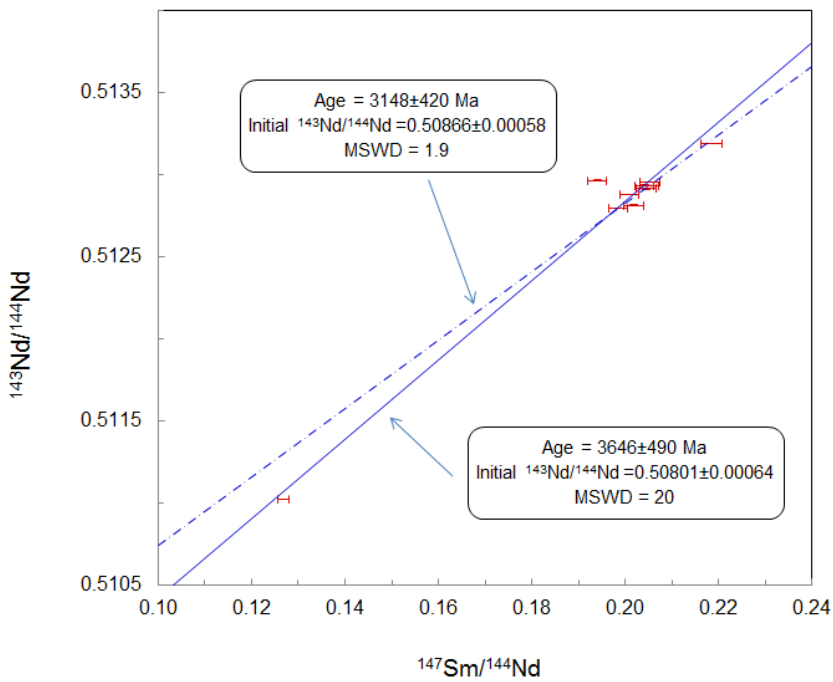


Figure S-13 $^{143}\text{Nd}/^{144}\text{Nd}$ vs. $^{147}\text{Sm}/^{144}\text{Nd}$ diagram for all Ameralik dykes (solid line) that show a high degree of scatter. Excluding samples that fall off the regression line as well as AM-17 that show evidence for contamination from host gneisses define a well-correlated regression with an age consistent within error of the U-Pb ages for Ameralik dyke emplacement.



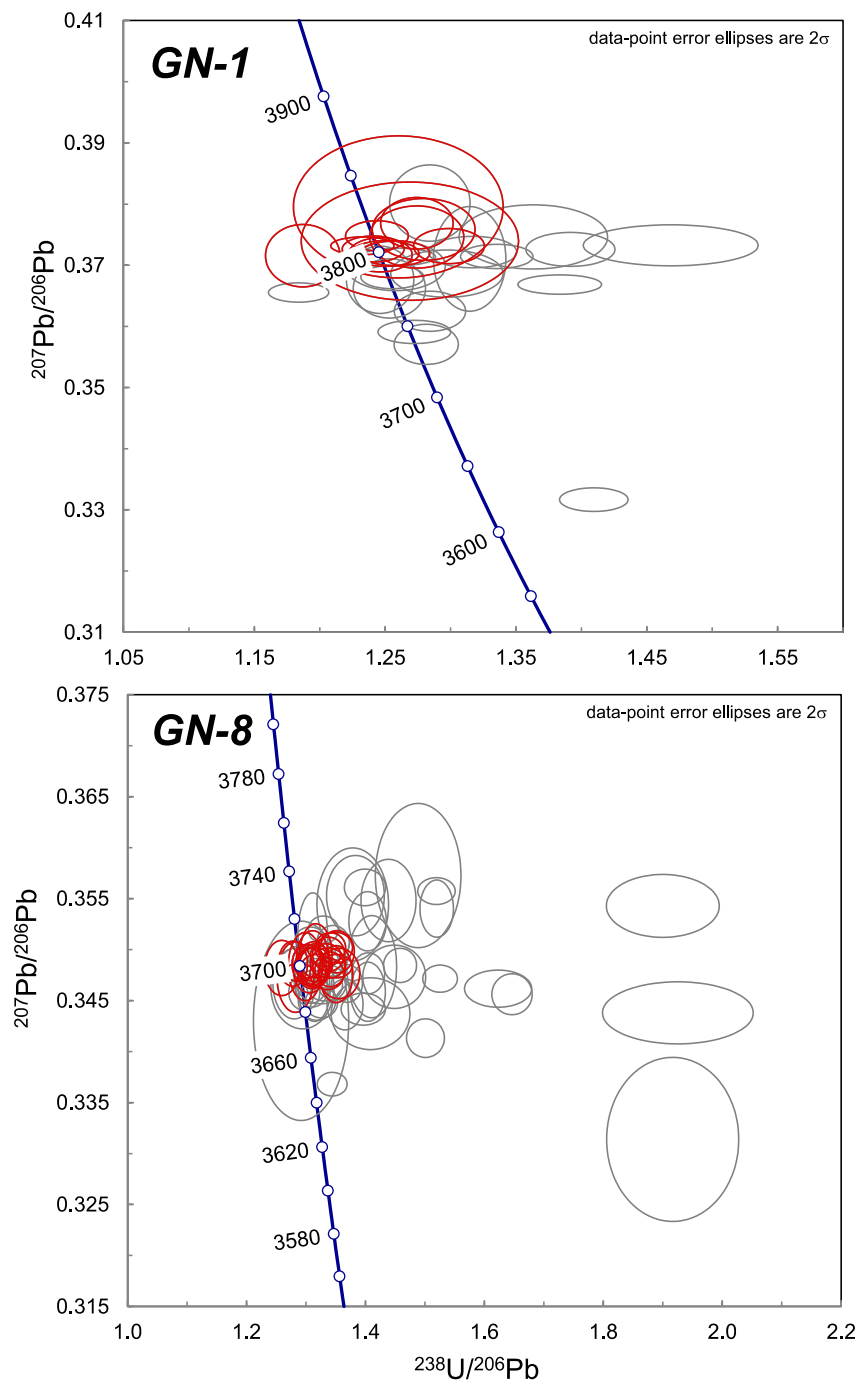


Figure S-14 Inverse concordia diagram for zircons from sample GN-1 and GN-8.



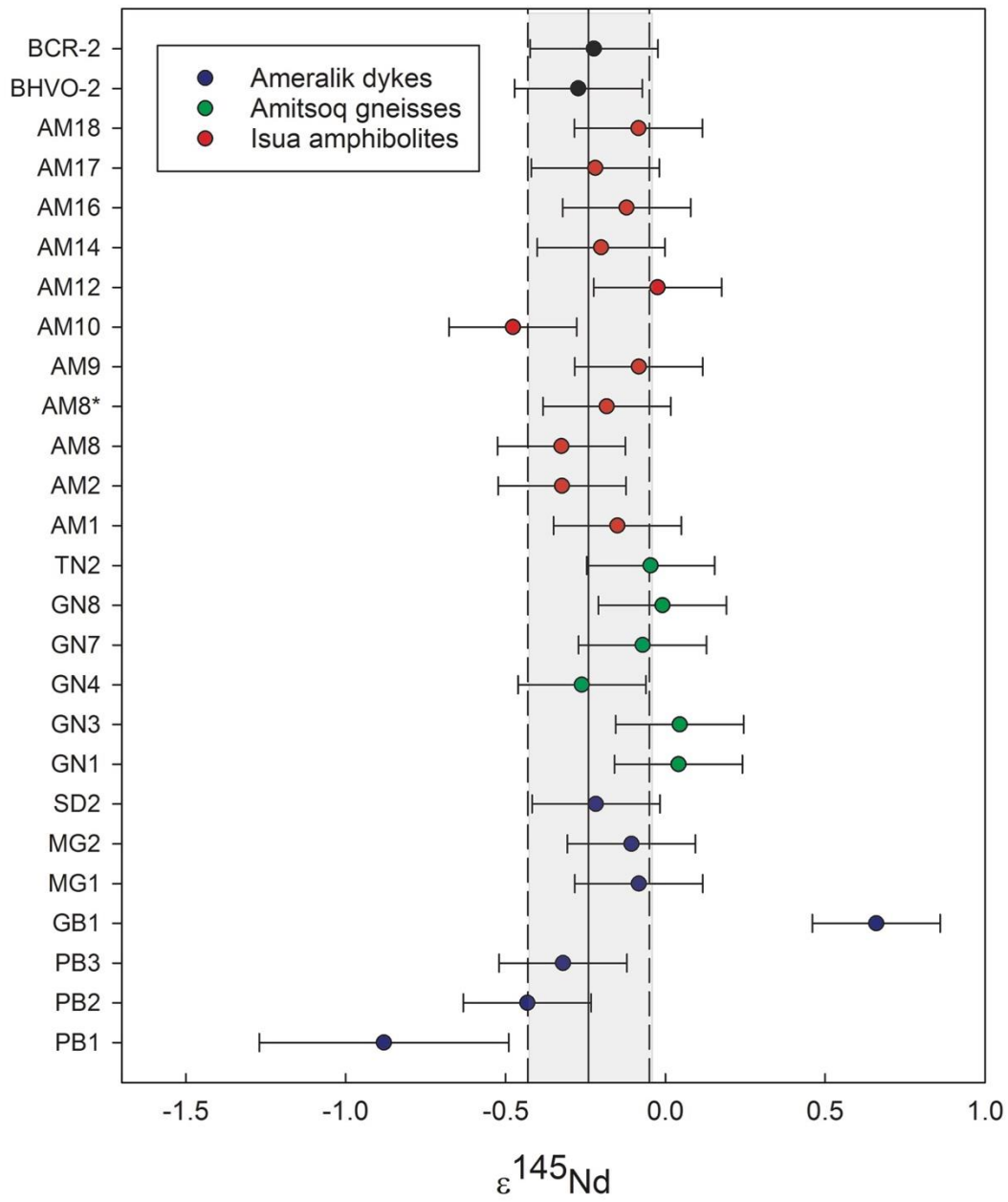


Figure S-15 Mass-dependent compositions *per* atomic mass unit measured for samples analysed in the study given as $\epsilon^{145}\text{Nd}$ values.



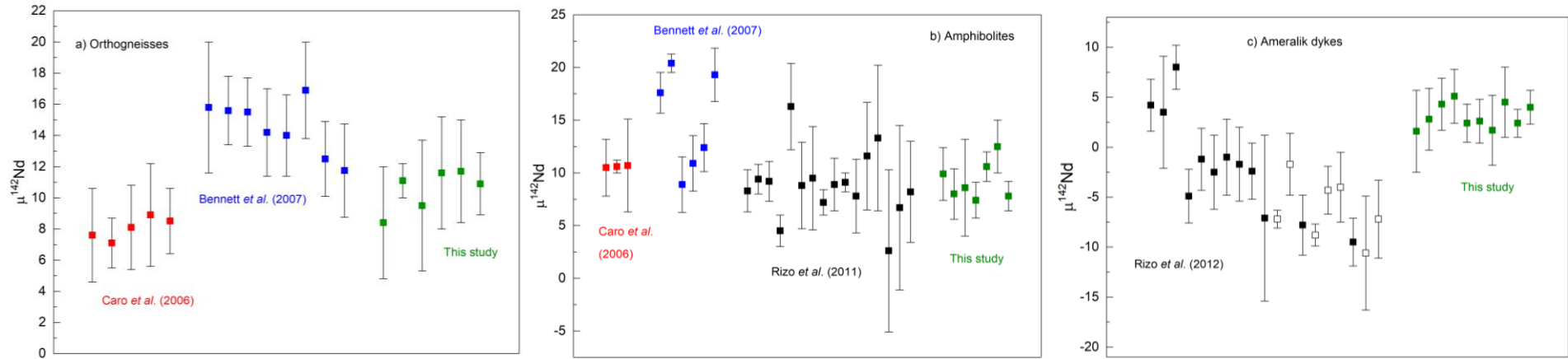


Figure S-16 Comparison of $\mu^{142}\text{Nd}$ values measured in this study with literature data for orthogneisses in **(a)**, amphibolites/metabasalts in **(b)** and Ameralik dykes in **(c)**. Data for orthogneisses and amphibolites is from Caro *et al.* (2006), Bennett *et al.* (2007) and Rizo *et al.* (2011). Data for Ameralik dykes is from Rizo *et al.* (2012). Uncertainties for literature data are 2σ errors. Note that $\mu^{142}\text{Nd}$ values are reported relative to Ames Nd isotope standard in Caro *et al.* (2006) and Bennett *et al.* (2007). Data from Rizo *et al.* (2011) and Rizo *et al.* (2012) is relative to JNdi-1 as in this study.



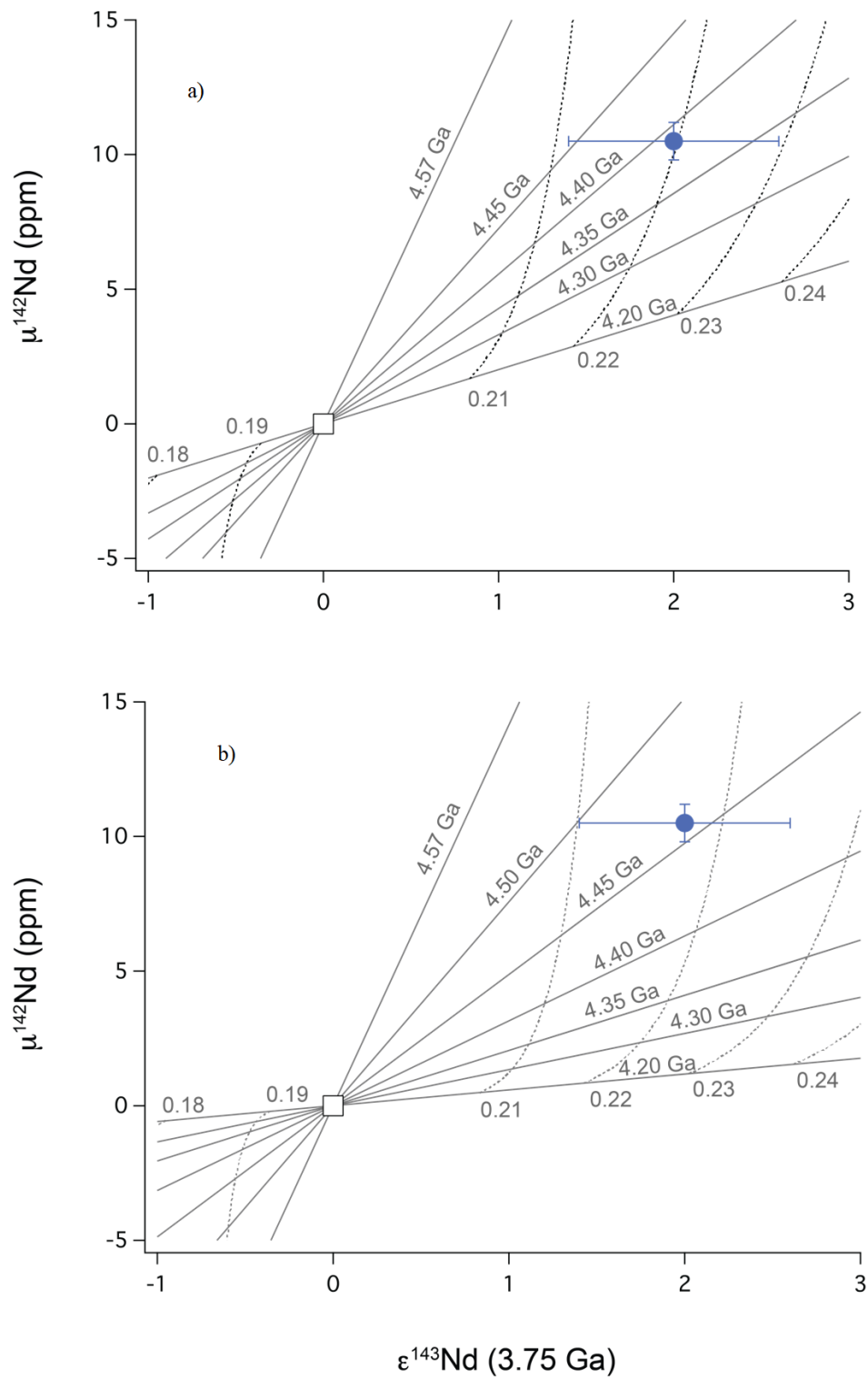


Figure S-17 The ^{142}Nd - ^{143}Nd coupled systematics for Isua supracrustal rocks using the ^{146}Sm half-life of 103 Myr in (a) and 68 Myrs in (b).



Supplementary Information References

- Bennett, V.C., Brandon, A.D., Nutman, A.P. (2007) Coupled ^{142}Nd - ^{143}Nd isotopic evidence for hadean mantle dynamics. *Science* 318, 1907-1910.
- Burkhardt, C., Borg, L.E., Brennecke, G.A., Shollenberger, Q.R., Dauphas, N., Kleine, T. (2016) A nucleosynthetic origin for the earth's anomalous ^{142}Nd composition. *Nature* 537, 394-398.
- Caro, G., Bourdon, B., Birck, J.-L., Moorbath, S. (2006) High-precision $^{142}\text{Nd}/^{144}\text{Nd}$ measurements in terrestrial rocks: Constraints on the early differentiation of the earth's mantle. *Geochimica et Cosmochimica Acta*, 70, 164-191.
- Condie, K.C. (2003) Incompatible element ratios in oceanic basalts and komatiites: Tracking deep mantle sources and continental growth rates with time. *Geochemistry, Geophysics, Geosystems* 4,1-28.
- Jacobsen, S.B., Yu, G. (2015) Extinct isotope heterogeneities in the mantles of earth and mars: Implications for mantle stirring rates. *Meteoritics & Planetary Science* 50, 555-567.
- Kellogg, J.B., Jacobsen, S.B., O'Connell, R.J. (2002) Modeling the distribution of isotopic ratios in geochemical reservoirs. *Earth and Planetary Science Letters* 204, 183-202.
- McDonough, W. F., Sun, S. s. (1995) The composition of the earth. *Chemical Geology* 120, 223-253.
- McLeod, C.L., Brandon, A.D., Armytage, R.M.G. (2014) Constraints on the formation age and evolution of the Moon from ^{142}Nd - ^{143}Nd systematics of Apollo 12 basalts. *Earth and Planetary Science Letters* 396, 179-189.
- Moorbath, S., Whitehouse, M.J., Kamber, B.S. (1997) Extreme Nd-isotope heterogeneity in the early Archaean-fact or fiction? Case histories from northern Canada and West Greenland. *Chemical Geology* 135, 213-231.
- Nutman, A.P., Friend, C.R.L. (2009) New 1:20,000 scale geological maps, synthesis and history of investigation of the isua supracrustal belt and adjacent orthogneisses, Southern West Greenland: A glimpse of eoarchaean crust formation and orogeny. *Precambrian Research* 172, 189-211.
- O'Neil, J., Rizo, H., Boyet, M., Carlson, R.W., Rosing, M.T. (2016) Geochemistry and nd isotopic characteristics of Earth's Hadean mantle and primitive crust. *Earth and Planetary Science Letters* 442, 194-205.
- Pearce, J. A. (2008). Geochemical fingerprinting of oceanic basalts with applications to ophiolite classification and the search for Archean oceanic crust. *Lithos* 100, 14-48.
- Polat, A., Hofmann, A.W., Rosing, M.T. (2002) Boninite-like volcanic rocks in the 3.7-3.8 Ga Isua greenstone belt, West Greenland: geochemical evidence for intra-oceanic subduction zone processes in the early earth. *Chemical Geology* 184, 231-254.
- Rizo H., Boyet, M., Blichert-Toft, J., O'Neil, J., Rosing, M.T., Paquette, J.-L. (2012) The elusive hadean enriched reservoir revealed by ^{142}Nd deficits in isua archaean rocks. *Nature* 491, 96-100.
- Rosing, M.T. (1990) The theoretical effect of metasomatism on Sm-Nd isotopic systems. *Geochimica et Cosmochimica Acta* 54, 1337-1341.
- Saji, N.S., Wielandt, D., Paton, C., Bizzarro, M. (2016) Ultra-high-precision Nd-isotope measurements of geological materials by MC-ICPMS. *Journal of Analytical Atomic Spectrometry* 31, 1490-1504.
- Stacey, J.S., Kramers, J.D. (1975) Approximation of terrestrial lead isotope evolution by a two-stage model. *Earth and Planetary Science Letters* 26, 207-221.
- Whitehouse, M.J., Kamber, B. (2005) Assigning dates to thin gneissic veins in high-grade metamorphic terranes: A cautionary tale from Akilia, Southwest Greenland. *Journal of Petrology* 46, 291-318.
- Wiedenbeck, M., Allé, P., Corfu, F., Griffin, W.L., Meier, M., Oberli, F., von Quadt, A., Roddick, J.C., Spiegel, W. (1995) Three natural zircon standards for U-Th-Pb, Lu-Hf, trace element and REE analyses. *Geostandards Newsletter* 19, 1-23.

